Check for updates

DISEASE AND DISORDERS

Single-cell multiome and spatial profiling reveals pancreas cell type-specific gene regulatory programs of type 1 diabetes progression

Rebecca Melton¹†, Sara Jimenez²†, Weston Elison¹, Luca Tucciarone³, Abigail Howell³, Gaowei Wang³, Denise Berti³, Elisha Beebe³, Michael Miller⁴, Chun Zeng³, Carolyn McGrail¹, Kennedy VanderStel³, Katha Korgaonkar³, Ruth Elgamal¹, Hannah Mummey⁵, Joshua Chiou⁶, Emily Griffin³, Irina Kusmartseva⁷, Mark Atkinson⁷, Sebastian Preissl^{4,8,9,10,11}, Fabian J. Theis²‡, Maike Sander^{3,12,13}‡, Kyle J. Gaulton³*‡

Cell type–specific regulatory programs that drive type 1 diabetes (T1D) in the pancreas are poorly understood. Here, we performed single-nucleus multiomics and spatial transcriptomics in up to 32 nondiabetic (ND), autoantibodypositive (AAB⁺), and T1D pancreas donors. Genomic profiles from 853,005 cells mapped to 12 pancreatic cell types, including multiple exocrine subtypes. β , Acinar, and other cell types, and related cellular niches, had altered abundance and gene activity in T1D progression, including distinct pathways altered in AAB⁺ compared to T1D. We identified epigenomic drivers of gene activity in T1D and AAB⁺ which, combined with genetic association, revealed causal pathways of T1D risk including antigen presentation in β cells. Last, single-cell and spatial profiles together revealed widespread changes in cell-cell signaling in T1D including signals affecting β cell regulation. Overall, these results revealed drivers of T1D in the pancreas, which form the basis for therapeutic targets for disease prevention.

Copyright © 2025 The
Authors, some rights
reserved; exclusive
licensee American
Association for the
Advancement of
Science. No claim to
original U.S.
Government Works.
Distributed under a
Creative Commons
Attribution
NonCommercial
License 4.0 (CC BY-NC).

INTRODUCTION

Type 1 diabetes (T1D) is a complex endocrine disorder characterized by autoimmune destruction of β cells in the pancreatic islets, leading to lifelong dependence on insulin therapy. The destruction of β cells in T1D is caused by interactions with multiple cell types in and surrounding the islet microenvironment including infiltrating immune cells, other endocrine cells, and endothelial cells (1–3). Cell types in the pancreas outside the local islet environment, such as exocrine acinar and ductal cells, are also increasingly implicated in T1D pathogenesis (4, 5). β Cells themselves likely contribute to the development of T1D as well through response to environmental factors, external signaling to immune, β , and other cell types, and cellular survival (6). The sequence of events in the pancreas that drives initiation of β cell autoimmunity and progression through stages of T1D, however, as well as the role of each pancreatic cell type in these processes, remains poorly understood.

¹Biomedical Sciences Program, University of California San Diego, La Jolla, CA, USA. ²Department of Computational Health, Institute of Computational Biology, Helmholtz, Munich, Germany. ³Department of Pediatrics, University of California San Diego, La Jolla, CA, USA. ⁴Center for Epigenomics, University of California San Diego, La Jolla, CA, USA. ⁵Bioinformatics and Systems Biology Program, University of California San Diego, La Jolla, CA, USA. ⁶Pfizer Research and Discovery, Pfizer Inc., Cambridge, MA, USA. ⁷Department of Pathology, Immunology and Laboratory Medicine, University of Florida, Gainesville, FL, USA. ⁸Institute of Experimental and Clinical Pharmacology and Toxicology, Faculty of Medicine, University of Freiburg, Freiburg, Germany. ¹⁰ClBSS-Centre for Integrative Biological Signalling Studies, University of Freiburg, Freiburg, Germany. ¹⁰Department of Pharmacology and Toxicology, Institute of Pharmaceutical Sciences, University of Graz, Graz, Austria. ¹¹Field of Excellence BioHealth, University of Graz, Graz, Austria. ¹²Department of Cellular and Molecular Medicine, University of California San Diego, La Jolla, CA, USA. ¹³Max Delbrück Center for Molecular Medicine, Berlin, Germany.

Seroconversion to autoantibody positivity (AAB⁺) against islet proteins (i.e., self-antigens) precedes T1D onset in nearly all cases and is used as a clinical biomarker of T1D progression (7, 8). Individuals at T1D diagnosis can present with a differing number and type of autoantibodies, which are associated with varying rates of disease incidence; for example, the presence of a single islet AAB has a relatively low lifetime risk of T1D, whereas individuals with multiple AAB have disease rates more than 90% (9-11). As clinical presentation of T1D does not occur until a large fraction of β cells has been destroyed, there is a window of time between seroconversion and T1D onset where disease processes can potentially be halted or reversed (7). Even after onset of T1D, residual β cell mass could potentially be modulated therapeutically to restore metabolic function (12). Defining changes in disease-relevant cell types across the stages of T1D progression would both improve our understanding of the mechanisms of T1D as well as reveal potential targets to prevent or reverse disease. Furthermore, an improved understanding of key changes associated with progression would also help identify biomarkers of T1D, which are particularly needed in the early stages of disease to identify progressors and candidates for therapeutic intervention (13).

Single-cell technology, the focus of this work, enables profiling of individual cells within the pancreas (5, 14). Previous single-cell studies of the pancreas in T1D have been limited in that they focused primarily on gene expression profiling of dispersed cells (4, 15), which does not provide information on the spatial localization of cellular transcriptomes within the pancreas nor the genomic elements driving changes in gene activity. Recent developments in spatial transcriptomics enables profiling cells in their native location (16), which enables understanding cell type–specific changes in the context of specific cellular neighborhoods and niches in the pancreas. This is particularly important in the context of T1D which has extensive heterogeneity in disease processes within the pancreas (17). In addition, single-cell epigenome profiling, for example, using

^{*}Corresponding author. Email: kgaulton@ucsd.edu

[†]These authors contributed equally to this work.

[‡]These authors contributed equally to this work.

single-nucleus Assay for Transposase-Accessible Chromatin using Sequencing (snATAC-seq) or single-cell multiome [paired single-nucleus RNA sequencing (snRNA-seq) + snATAC-seq], can reveal transcriptional regulators, cis-regulatory elements (cREs), and gene regulatory networks (GRNs) driving altered gene expression in T1D (14, 15). Critically, GRNs and cREs can be intersected with T1D-associated variation to infer cell type–specific regulatory programs that may play a causal role in driving disease (5, 18).

Previous single-cell studies have also been limited in the extent to which they have captured key windows of T1D progression and pathogenesis (4, 15). Specifically, nondiabetic (ND) AAB⁺ donors in these efforts were largely those with single glutamic acid decarboxylase (GAD) autoantibodies (4), which have a relatively lower risk of developing T1D compared to multiple AAB⁺ donors and do not reflect the full arc of progression to T1D (19). Furthermore, many of the T1D donors in these studies had long-standing T1D where disease processes are potentially more dormant, whereas profiling donors who had more recently developed T1D may give greater insight into active disease processes. Third, these studies profiled purified islets, and profiling tissue sampled from the whole pancreas may offer greater insight into genomic changes during T1D progression in exocrine cells and other cell types outside of the islet microenvironment.

In this study, we addressed these limitations by performing single-cell gene expression and epigenome profiling in whole pancreas from 32 ND, ND single and multiple AAB⁺, recent-onset T1D, and long-standing T1D organ donors, as well as spatial transcriptomics in a subset of ND and recent-onset T1D donors. We determined changes in pancreatic cell type abundance, cellular pathways, GRNs, and cell-cell signaling across these stages of T1D progression and pathogenesis and, using T1D association data, identified pathways and gene networks that may play a causal role in the development of T1D.

RESULTS

A comprehensive, multimodal, spatially resolved map of pancreatic cell types

We obtained pancreatic tissue from 32 donors in the Network for Pancreatic Organ Donors with Diabetes (nPOD) biorepository including 11 ND, 9 ND autoantibody positive (ND AAB⁺), and 12 T1D which we separated into 7 recent onset (<1 year from diagnosis) and 5 longer duration (>5 years from diagnosis) (table S1). Within the ND AAB⁺ group, most organ donors, by our study design, had multiple autoantibodies (multiple ND AAB⁺). For all samples, we performed snRNA-seq and snATAC-seq assays, and for eight of the samples, we performed single-nucleus multiome (joint snRNA-seq and snATAC-seq in the same nucleus) assays (table S1). In addition, for six of the samples, we performed spatial transcriptomic assays using the CosMx Spatial Molecular Imager (Fig. 1A).

After extensive barcode quality control and filtering steps (see Materials and Methods), we integrated data from all 32 donors using Harmony (20) and clustered 276,906 gene expression profiles (Fig. 1B and figs. S1 and S2). We annotated the resulting 18 clusters based on the expression of known cell type marker genes which revealed 12 pancreatic cell types including exocrine (acinar and ductal), endocrine (α , β , and δ), immune (T cell, B cell, macrophage, and mast), stellate, endothelial, and Schwann cells (Fig. 1, B and C, and table S2). Cell type clusters had broadly consistent representation

across donors and donor characteristics (figs. S2 and S3). We aggregated expression profiles for all cells in the cell type and derived normalized expression levels of each gene using counts per million (CPM) (data S1). For each cell type, we further identified genes with expression levels specific [false discovery rate (FDR) < 0.1] to the cell type which revealed both known and previously unreported sets of genes with cell type–specific expression (table S3); for example, well-known genes with expression specific to β cells included *INS*, *IAPP*, and *G6PC2* as well as others with no now known role in β cell function (e.g., *PLCH2*, *NRG2*, *RBFOX3*, and *MTUS2*).

Several cell types displayed multiple subclusters representing both known cell subtypes, such as active and quiescent stellate cells, blood vessel cells (BVECs), lymphatic endothelial cells (LECs), and MUC5b⁺ ductal cells, as well as several potential subtypes of acinar cells (Fig. 1, B and C). As the genomic properties of these subtypes have not been completely described previously, we derived sets of marker genes for each subtype (see Materials and Methods and table S3). For BVECs and LECs, in addition to reported marker genes PLVAP (BVECs) and FLT4 (LECs), we observed specific upregulation of genes in each subtype such as INHBB, BMP6, FCN3, and PCAT19 in BVECs and EFNA5, COLEC12, and MYCT1 in LECs. In MUCB5⁺ ductal cells, there was up-regulation of ERN2, CYP2C18, MYO7B, and DMBT1 compared to the primary subtype of ductal cells. For acinar cells, the primary cluster, which we annotated as "basal" acinar cells, was enriched for genes and pathways involved in digestive enzyme production and secretion. Other clusters included "high-enzyme" acinar cells with higher expression of enzymes such as chymotrypsin (CTRB1/2), trypsinogen (PRSS1 and PRSS2), lipase (PNLIP), carboxyl ester lipase (CEL), chymotrypsinlike elastase (CELA3A/B), and increased oxidative phosphorylation and translation, "signaling" acinar cells with increased signaling and stress-response activity, and "signaling/differentiation" acinar cells with increased signaling, metallothionein (MT1/MT2), and identity and differentiation genes (REG1A/B and PTF1A) (Fig. 1D).

To next characterize the spatial organization of pancreatic cell types, we performed RNA in situ hybridization of 1010 genes with CosMx from a subset of donors including three ND and three recent-onset T1D (tables S1 and S4). We imaged a total of 82.6M transcripts from 71 fields of view (FOVs) in pancreatic sections from three ND (32 FOVs) and three recent-onset T1D donors (39 FOVs) (fig. S4A) and assigned transcripts to 392,248 cells overall (80 median genes and 200 median transcripts per cell), using the CosMx default segmentation. We performed unsupervised clustering of cellular gene expression profiles, which revealed nine distinct clusters including exocrine, endocrine, endothelial, immune, and mast cells (fig. S4B). We next mapped finer-grained cell type annotations from snRNA-seq using moscot (fig. S4, B and C) (21), which revealed 14 cell types and subtypes that were confirmed on the basis of marker gene expression (Fig. 1E and fig. S4). Spatial neighborhood enrichment using squidpy (22) revealed expected cell type clustering including acinar subtypes, ductal subtypes, endocrine cells (β , α , and δ), and connective cells (e.g., endothelial, immune, and stellate) (Fig. 1F).

Next, we sought to determine whether spatial neighborhoods form recurrent niches across the pancreas, by defining niches involving a cell type using a gene-gene covariance matrix (23) in a spatial neighborhood of 30 cells. We recovered six niches in total, characterized by cell type abundance (see Materials and Methods), including three exocrine (acinar-enriched, ductal-enriched, and

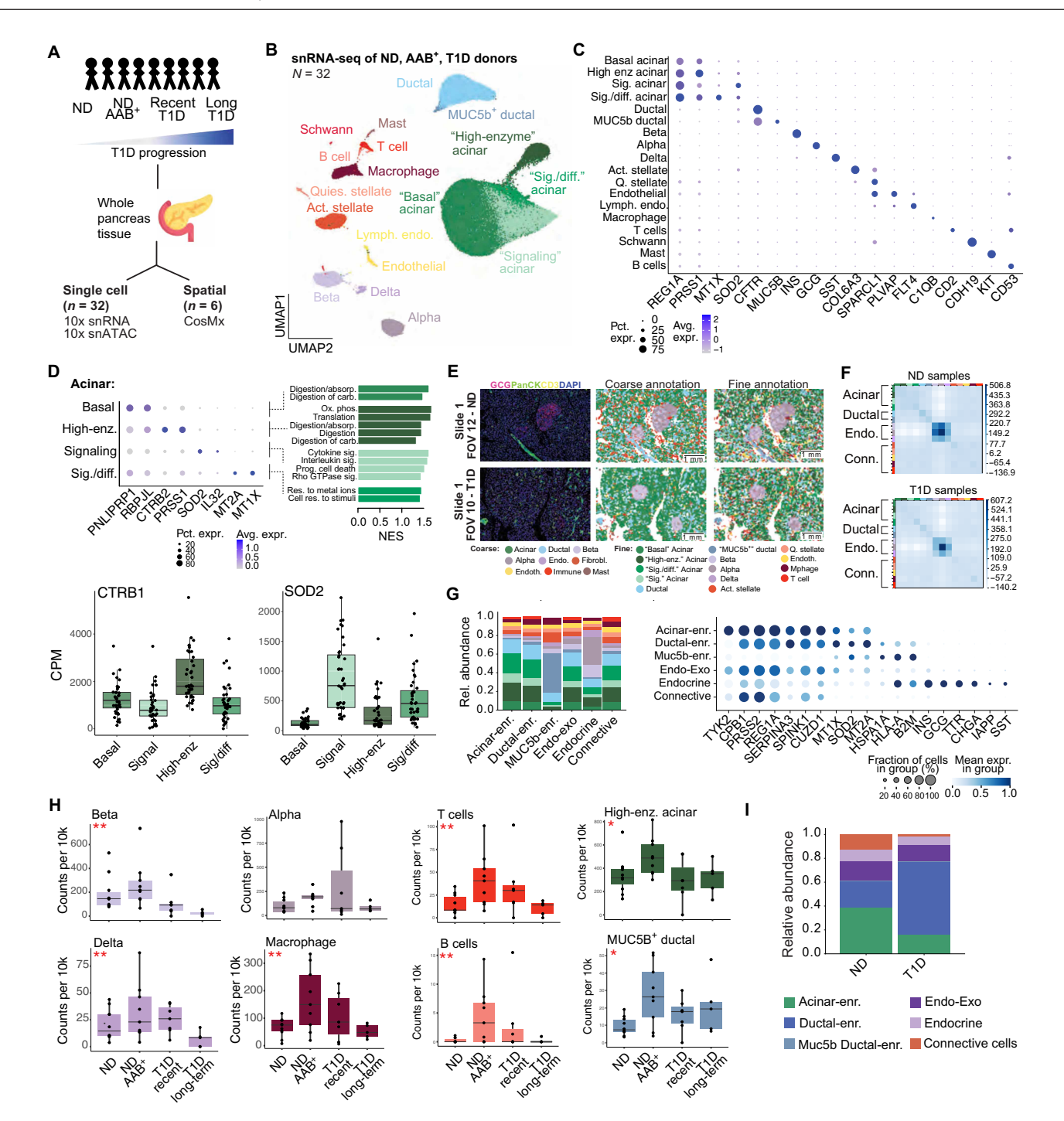


Fig. 1. Cell type–specific map of gene expression in the pancreas. (A) Design of study profiling human pancreas from ND, ND AAB⁺, and T1D donors using single-cell assays. (B) Uniform Manifold Approximation and Projection (UMAP) plot showing clustering of 276,906 nuclei from single-nuclear RNA-seq of 32 whole pancreas donors from the nPOD biorepository. Clusters are labeled on the basis of cell type and subtype annotations. (C) Dot plot showing the normalized expression levels of selected known marker genes for pancreatic cell types and subtypes. (D) Dot plot of genes with preferential expression across different subtypes of acinar cells (top left) and normalized enrichment score (NES) of pathways enriched in each subtype using fgsea (top right). Box plot showing donor CPM of selected genes with preferential expression in different subtypes of acinar cells. GTPase, guanosine triphosphatase. (E) Representative FOV per condition (ND: top, T1D: bottom) showing (from left to right) immunofluorescence, coarse cell type annotation with the spatial gene panel directly, and finer-grained cell type annotation transferred from the snRNA-seq data. DAPI, 4',6-diamidino-2-phenylindole. (F) Matrix plots showing the neighborhood enrichment of cell types based on spatial neighbors. Cell type labels are the same as fine-grained annotations in (E). (G) Stacked barplot illustrating the relative abundance of each cell type in each multicellular niche. Cell type labels are the same as fine-grained annotations in (E, left). Dot plot showing the normalized gene expression levels of spatially variable genes across multicellular pancreatic niches (right). (H) Box plot showing normalized cell counts for selected pancreatic cell types and subtypes grouped by T1D status. P values from likelihood ratio test, **FDR < 0.1, *uncorrected P < 0.05. (I) Stacked barplot showing the relative abundance of each multicellular niche per condition. Niches have altered abundance in ND samples denoted as *P < 0.05.

MUC5b ductal-enriched) niches, one endocrine niche, one niche including both endocrine and exocrine cells (endo-exo), and one niche consisting of connective cells (Fig. 1G). To characterize each niche, we identified spatially variable genes (Moran's I > 0.2, P < 0.05) that captured gene signatures specific to the niche (Fig. 1G). In the acinar-enriched niche, marker genes from the basal and high-enzyme cell types showed strong spatial clustering (PRSS2 and REG1A). In comparison, the ductal-enriched niche had more spatial association with signaling and signaling/differentiation acinar cells (MT1X, SOD2, and MT2A). In the MUC5b ductal-enriched niche, spatially variable genes were strongly associated with immune interactions (HSPA1A, HLA-A, and B2M). In addition, the endocrine niche had highly distinct patterns which highlighted multiple endocrine-specific genes (e.g., INS, GCG, SST, and IAPP) (Fig. 1G).

Last, we determined whether there were changes in abundance of cell types and subtypes in T1D progression based on snRNA-seq (see Materials and Methods). There was a significant decrease (likelihood ratio test, FDR < 0.1) in β cells (Fig. 1H and table S5) although we still observed residual β cells in T1D particularly in recent-onset (ND = 1.5%, recent-onset T1D = 0.93%). We also observed a significant decrease (FDR < 0.1) in δ cells in T1D and increased abundance of immune populations in ND AAB⁺ and recent-onset T1D. There was also nominal evidence (P < 0.05) for altered abundance of specific subtypes including high-enzyme acinar (P = 0.037) and MUC5b⁺ ductal cells (P = 0.049). We next asked whether there were corresponding changes in the abundance of specific niches in T1D in spatial profiles. We quantified the pairwise similarity between ND and T1D spatial graphs using Wasserstein distance (fig. S4D) (24), which revealed substantial changes in the underlying structure of endocrine cells (α and β) in T1D. We also observed significant changes in the abundance of the endocrine and $MUC5b^{+}$ ductal niche in T1D (P < 0.05) (Fig. 1I).

Comprehensive map of pancreatic cell type-accessible chromatin

To understand how the epigenome may drive changes in cell typespecific gene expression in T1D, we next created a matched map of accessible chromatin in pancreatic cell types. Of the 32 nPOD donors with snATAC-seq assays, 30 passed quality control (see Materials and Methods). We filtered, integrated, and clustered accessible chromatin profiles from the 30 donors and annotated cell type identity by label transfer of the gene expression map using Seurat (see Materials and Methods) (25). After filtering nuclei with low transfer predictions (<0.5), there were 203,348 chromatin profiles mapping to the same cell types and subtypes (Fig. 2A and figs. S6 and S7). We estimated that label transfer was >97% accurate at the cell type level by comparing the predicted and actual identity of accessible chromatin profiles in single-cell multiome data. We also confirmed that predicted cell types were accessible at the promoter regions of key marker genes (Fig. 2B). The proportions of each cell type were highly correlated between expression and chromatin maps (r = 0.98, $P = 1.7 \times 10^{-13}$; fig. S8).

We identified transcription factor (TF) binding motifs preferentially enriched in each pancreatic cell type and subtype using chrom-VAR (26). At the cell type level, enriched sequence motifs revealed key regulators of each cell type; for example, β cells and other endocrine cells were enriched for RFX and FOXA motifs; ductal cells for HNF1, ONECUT, and TEAD motifs; endothelial cells for ETV, FLI, and GABPA motifs; and T cells for RUNX, ETV, and ETS motifs,

among others (Fig. 2C and table S6). Motif enrichments also highlighted regulators that distinguished accessible chromatin profiles of cell types within specific lineages; for example, NEUROD1 and NR3C1 had stronger enrichment in β compared to other endocrine cells (Fig. 2C). Acinar cells showed distinct sets of enriched TF motifs across different subclusters, including signaling acinar cells which were more enriched for FOS/JUN, activating transcription factor (ATF), and Nuclear Factor Erythroid (NFE) motifs (Fig. 2, C and D, and table S6). In high-enzyme acinar cells, the strongest enrichments were for TFs such as Zinc finger E-box-binding (ZEB), Snail transcription factor (SNAI1-3), and Transcription Factor (TCF3-4), which were also the most enriched motifs in acinar cells overall compared to other cell types (Fig. 2, C and D, and table S6). As structurally related TFs often have similar motifs, we linked TF motifs enriched in subclusters to specific TFs in the same structural subfamily with concordant expression patterns. For example, FOSL2 and JUNB/D, as well as ATF3, NFE2L2, and BACH1/2, were increased in signaling acinar cells (Fig. 2D).

For each cell type and subtype, we next defined candidate cREs. We derived "pseudo"-bulk accessible chromatin profiles by aggregating reads from all cells for that cell type or subtype and identified cREs by performing peak calling with Model-based Analysis of ChIP-seq (MACS2). In total, there were 368,688 cREs across cell types and an average of 94.3k cis-regulatory elements (cREs) per cell type (data S2). Among cREs in our study, 9.4 and 7.4% were unique

type (data S2). Among cREs in our study, 9.4 and 7.4% were unique compared to a pan-tissue (27) and pancreas-specific (5) cRE catalog, respectively, such as a T cell cRE directly upstream of ZNF746 (Fig. 2E). We identified cREs with cell type–specific activity by comparing accessible chromatin profiles across cell types (data S3; see Materials and Methods). Cell type-specific cREs were enriched for sequence motifs of key cell type TFs as well as proximity to genes involved in cell type-specific function (tables S7 and S8). For example, β cell–specific cREs were significantly enriched (FDR < 0.1) for proximity to insulin secretion-related pathways and RFX, FOXA, NEUROD, and NKX6.1 TF motifs, whereas endothelial-specific cREs were significantly enriched for proximity to angiogenesis, blood vessel morphogenesis, and vasculature pathways and FLI, ETS, and ETV TF motifs (tables S7 and S8). We also identified cREs specific to several of the subtypes within acinar cells; for example, signaling acinar-specific cREs were enriched for JUN, FOS, and ATF motifs.

Because of the scarcity of immune populations in the pancreas, the epigenome of resident and infiltrating pancreatic immune cells has not been extensively described. In our study, we identified multiple immune cell types including T cells, macrophages, B cells, and mast cells, although available cell numbers only enabled defining cREs in T cells and macrophages. T cell-specific cREs were significantly enriched for proximity to genes involved in T cell activation, T cell receptor complex, and cytokine receptor activity and motifs for ETS, ETV, and RUNX TFs, while macrophage-specific cREs were enriched for immune-related processes and PU.1 and SPIB motifs (Fig. 2F). Compared to a previous study which profiled several whole pancreas donors, more than double the number of cREs were identified in each cell type (T cells: 58.8k versus 24.5k; macrophages: 114.3k versus 55.7k). The increased number of cREs improved annotation of T1D-associated variants; for example, candidate T1D variant rs947474 [posterior probability of association (PPA) = 0.88] (5) overlapped a pancreatic T cell and macrophage cRE not

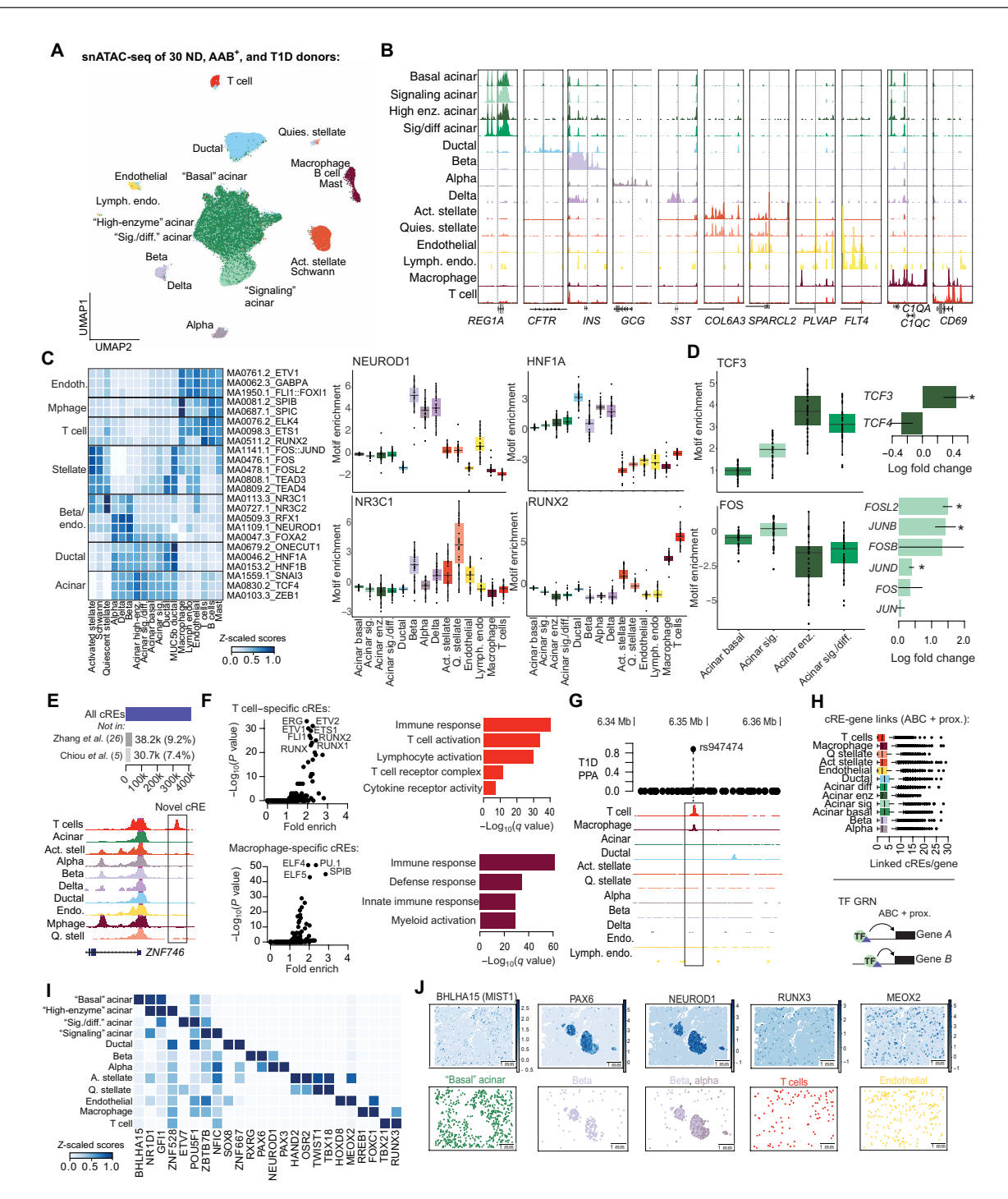


Fig. 2. Cell type–specific map of accessible chromatin in the pancreas. (A) UMAP plot showing clustering of 203,348 nuclei from single-nuclear ATAC-seq of 30 pancreas donors from the nPOD biorepository. Clusters are labeled with cell type and subtype identity based on label transfer from the gene expression map. (B) Genome browser showing accessible chromatin signal at the promoter regions of known marker genes for pancreatic cell types. (C) Heatmap showing genome-wide accessibility from chromVAR of sequence motifs for selected transcription factors (TFs) across cell types (left) and box plots showing donor-level accessibility of selected TF motifs across cell types (right). (D) Box plot showing genome-wide accessibility of TF motifs with preferential enrichment in subtypes of acinar cells (left) and log fold change in expression for genes in structural subfamilies for enriched TF motifs, and error bars are SE (right). *FDR < 0.10. (E) Number of cREs identified across all cell types and the percentage of cREs that do not overlap previous catalogs of cREs (27, 53) (top). Example of a pancreatic T cell–specific cRE at the ZNF746 locus. (F) TF sequence motifs enriched in cREs with activity specific to each cell type (left) and bar plots showing —log₁₀ P values of gene sets enriched for proximity to cell type—specific cREs using the Genomic Regions Enrichment of Annotations Tool (GREAT). (G) Example of a cRE active in pancreatic T cells and macrophages that overlaps a candidate T1D risk variant. (H) Box plot showing gene-cRE links per gene per cell type (top) and schematic of TF GRNs (bottom). (I) Matrix plot showing scaled z-score of TF activities for top TFs identified for each cell type using a t test with overestimated variance. (J) Spatial plot of selected TFs showing the TF activity profile (top) and cell type distribution for the respective cell type (bottom).

identified in these cell types in the pancreas previously and not active in other pancreatic cell types (Fig. 2G).

We next predicted networks of genes regulated by TF activity in each pancreatic cell type (see Materials and Methods). We linked cREs to target genes in each cell type using the activity-by-contact (ABC) method, which revealed an average of 46,474 cRE-target gene links per cell type, as well as based on promoter proximity (data S4). Using ABC and promoter proximity, genes were linked to, on average, 2.8 cREs per cell type (Fig. 2H). We identified genes which had highly cell type-specific cRE links (see Materials and Methods), and genes with highly cell type-specific cRE links included key marker genes such as INS in β cells, GCG in α cells, IL-2, IFNGR1, and GZMA in T cells, and MARCOS in macrophages. In each cell type, we next constructed GRNs for 366 TFs by combining (i) cRE-target gene links, (ii) TF motif predictions in cREs, and (ii) TF and target gene expression levels (Fig. 2H; see Materials and Methods and data S5). We annotated likely cellular functions of TF GRNs by identifying biological pathways with gene sets that significantly overlapped TF GRNs. There were thousands of significant relationships linking TF GRNs to biological pathways across all cell types (Fisher's test, FDR < 0.1) (data S6), which annotated many known regulators of pathway activity as well as many putative functions of TFs.

Last, we used spatial transcriptomic data in combination with cell type-specific TF GRNs to infer TF activity within cell types and subtypes in the pancreas. Briefly, we used a univariate linear model to predict the observed gene expression based on TF-gene interaction weights, from which we scored TFs as active or inactive in each cell type (28). We identified TFs with endocrine-specific activity in line with the previously described regulators of endocrine cell activity, such as NEUROD1, as well as high activity of PAX6 in β cells, where it is a key regulator of β cell identity, function, and survival (Fig. 2, I and J) (29). Among other cell types, we inferred high activity for BHLHA15/MIST1 in acinar cells, where it may play a role in the maintenance of pancreatic acinar identity (30), and highly specific activity for MEOX2 in endothelial cells and RUNX3 in T cells (Fig. 2, I and J). Integrating GRNs with spatial transcriptomic profiles thus confirmed the specificity of key TFs regulating pancreatic cell types, including for TFs not measured on the spatial panel directly.

Pancreatic cell type gene expression in T1D progression

Changes in genome-wide gene activity within each pancreatic cell type during progression to T1D are poorly understood. We therefore identified genes and biological pathways in each cell type with altered activity in ND AAB+ and T1D. To increase our power to detect changes in endocrine cell types, we also used single-cell RNAseq from purified islets of 48 donors from the Human Pancreas Analysis Program (HPAP) (4, 15, 31) including 27 ND, 11 ND AAB⁺ (9 single, 2 multiple), and 10 T1D (6 recent, 4 long-standing). For each cell type and subtype, we derived gene counts per sample, tested for differential expression in single and multiple ND AAB⁺ and recent and long-standing T1D compared to nondiabetes, and considered genes significant at FDR < 0.1 (see Materials and Methods). We further performed gene set enrichment of differential expression results for each cell type and subtype and identified pathways with significant (FDR < 0.1) changes in activity in each condition (see Materials and Methods).

Marked gene expression changes were observed in β cells in T1D (Fig. 3A). In recent-onset T1D, 704 genes in β cells had a

significant change (FDR < 0.1) in expression, where the most upregulated genes included major histocompatibility complex (MHC) class I and related (CD74 and B2M) genes, cytokines, and cytokineinduced genes (IL15, GBP2, and IFIT3), cytokine-responsive TFs (STAT1/4 and IRF1), and components of the 20S proteosome (Fig. 3B, fig. S9, and data S7). We also observed up-regulation of MHC class II genes in T1D, particularly HLA-DPB1, as well as MHC class 1 modulators such as NLRC5 (fig. S9). At the pathway level, there was up-regulation of antigen processing and presentation, interferon signaling, interleukin signaling, and Janus kinase-signal transducers and activators of transcription (JAK-STAT) signaling and down-regulation of oxidative phosphorylation, translation, mitochondrial function, mitosis, mRNA processing, protein folding and localization, endoplasmic reticulum (ER)-Golgi transport, and autophagy (Fig. 3C and table S9). We examined whether specific pathways up-regulated in T1D showed heterogeneity in expression across single β cells and pathways including antigen presentation had evidence for bimodal expression while others such as interferon and JAK-STAT signaling did not (fig. S10). Further, a higher proportion of β cells from ND AAB⁺ and T1D donors expressed antigen presentation pathways compared to ND (fig. S10).

Compared to recent-onset T1D, the most significant changes in gene expression generally differed in long-standing T1D, including down-regulation of *INS* and key genes involved in β cell function such as *GLIS3* and *G6PC2* (data S7). In addition, antigen presentation and class I MHC genes were less pronounced, specific IRF TFs had higher expression, and class II MHC genes had stronger upregulation in long-standing T1D (fig. S9). At the pathway level, interferon signaling was significantly enriched (FDR < 0.1) in long-standing T1D, although there were overall few pathways with significant changes in activity potentially due to the low number of β cells at this stage (table S9). We identified more nominal enrichment for multiple pathways including up-regulated antigen presentation and cytokine receptor interactions and down-regulated autophagy, insulin processing, β cell regulation, and β cell development (table S9).

Given marked changes in gene expression in β cells in recentonset T1D, we further characterized whether these pathways had altered activity within specific localizations in the pancreas. Of the genes with altered expression in β cells in recent onset T1D and present in the spatial gene panel, almost all (95%) were up-regulated in T1D in spatial profiles (Fig. 3D and fig. S11). Furthermore, multiple up-regulated genes in T1D such as MHC class I genes (e.g., HLA-A and B2M) showed spatially dependent expression patterns (Moran's I > 0.2) within endocrine, immune, and ductal cells (Fig. 3D). We further characterized pathways in recent-onset T1D with expression profiles dependent on specific niches and altered in T1D progression. We identified pathways in the PROGENy database in LIANA+ (32) to predict pathways preferentially active in a niche using a multivariate linear model. We identified multiple pathways with niche-dependent expression, including hypoxia in the endocrine niche (Fig. 3E). When further assessing T1D-specific changes, pathways related to hypoxia and inflammation such as tumor necrosis factor-α and JAK-STAT were differentially active in T1D (fig. S11).

In contrast to T1D, few individual genes had significant changes in expression in β cells in either single or multiple ND AAB⁺ (Fig. 3A). We determined whether more subtle changes might be occurring at these stages. Genes altered in recent-onset T1D had significantly

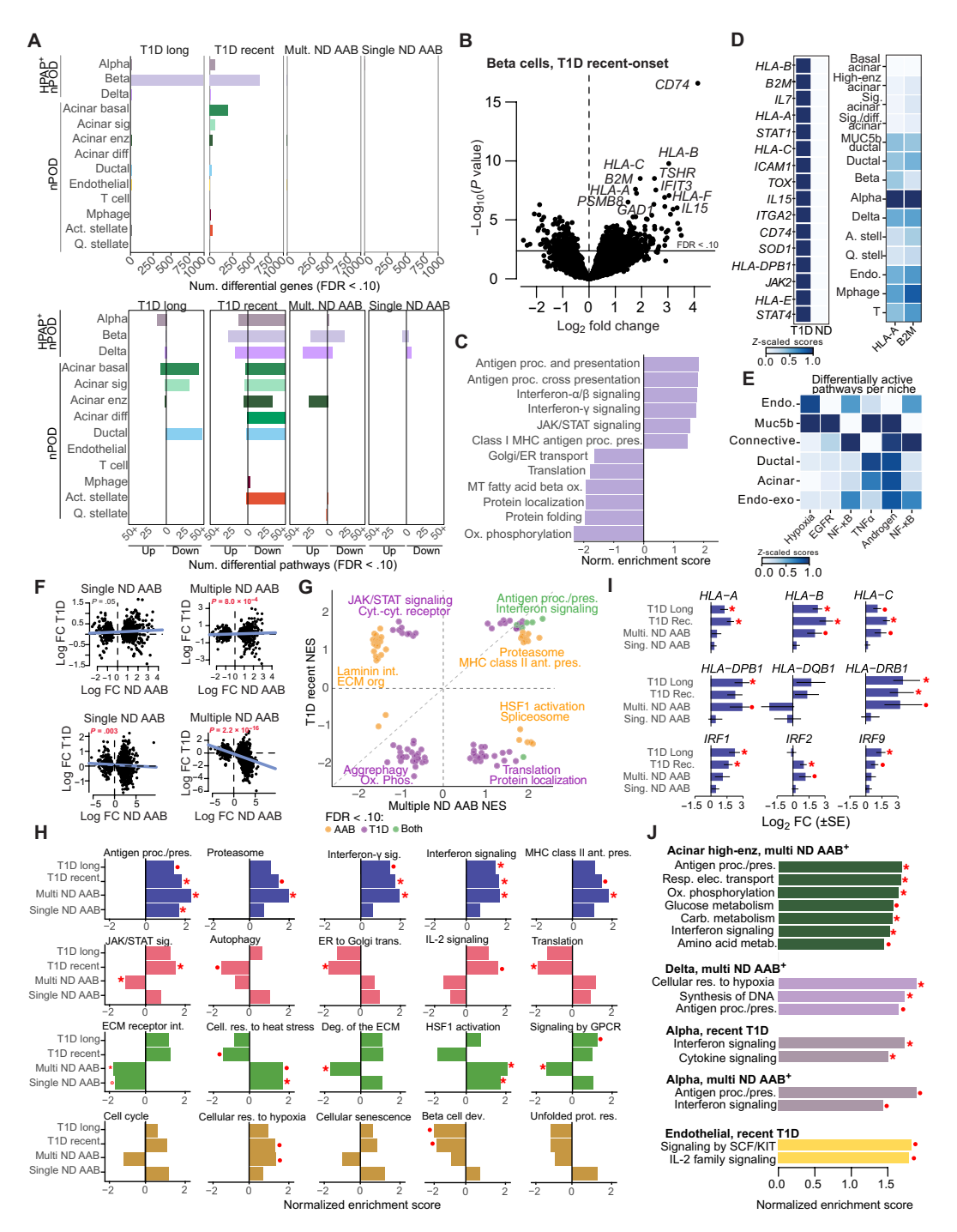


Fig. 3. Cell type—**specific changes in gene expression in T1D progression.** (**A**) Number of genes in each cell type with significant (FDR < 0.1) changes in expression in T1D stages compared to nondiabetes (top). Number of pathways enriched in genes with up- and down-regulated expression in each cell type in T1D stages (bottom). The results in all panels include 80 donors (nPOD + HPAP) for endocrine cells and 32 donors (nPOD) for nonendocrine cells. Note that nonendocrine cells were not tested for single ND AAB⁺ association. (**B**) Volcano plot showing differential expression in β cells in recent-onset T1D compared to ND. (**C**) Bar plot showing normalized enrichment (NES) of pathways enriched in up- and down-regulated genes in β cells in recent-onset T1D (bottom). MT, Mitochondrial. (**D**) Scaled expression in spatial profiles of genes with up-regulated expression in T1D in β cells (left). Spatially dependent expression of selected genes up-regulated in T1D in each cell type (right). (**E**) Pathways with differential expression within spatial niches in T1D compared to ND. EGFR, epidermal growth factor receptor; TNFα, tumor necrosis factor—α. (**F**) Scatterplot of log fold change in expression of genes in β cells in single or multiple ND AAB⁺ compared to recent-onset (top) and long-duration T1D (bottom). Line shown in each plot is from a linear model of log fold change values, and *P* values are from Spearman correlation. FC, fold change. (**G**) Normalized enrichment of pathways in recent-onset T1D and multiple ND AAB⁺. Pathways are colored on the basis of significant enrichment (FDR < 0.1) in either, or both, states. (**H**) Normalized enrichment of pathways in β cells across each T1D state compared to nondiabetes. (**I**) Log fold change in expression of selected genes in β cells in each T1D state compared to ND. (**J**) Normalized enrichment of pathways in other pancreatic cell types in recent-onset T1D or multiple ND AAB⁺. For all panels, *FDR < 0.1, 'P < 0.05.

correlated effects in multiple ND AAB+, although not in single ND AAB⁺ (Fig. 3F). At the pathway level, antigen processing and presentation were up-regulated in both single and multiple ND AAB⁺, and interferon signaling was up-regulated in multiple ND AAB+ (Fig. 3, G and H, and table S9). Among key genes in these pathways, MHC class I genes and interferon signaling IRF TFs were upregulated in multiple but not in single ND AAB+ (Fig. 3I and data S7). We also identified pathways altered specifically in single and multiple ND AAB⁺ and not in recent-onset T1D; for example, heat stress response was up-regulated in single and multiple ND AAB⁺, extracellular matrix (ECM) organization, cytokine-cytokine interactions, and G protein-coupled receptor (GPCR) ligand binding were all down-regulated in multiple ND AAB+, and transforming growth factor-β (TGF-β) signaling was down-regulated in single ND AAB⁺ (Fig. 3H and table S9). In addition, class II MHC antigen presentation was strongly up-regulated in multiple ND AAB⁺, but not in single ND AAB⁺, including class II MHC genes HLA-DBP1 and HLA-DRB1 (data S7 and table S9). These results highlight that single and multiple ND AAB+ have both shared and distinct genomic changes in β cells compared to T1D.

Changes have been reported in the exocrine pancreas in T1D and at-risk individuals (33), and in our study, we observed marked changes in exocrine cell gene expression in T1D progression. In basal acinar cells, there were 255 genes with altered expression in recent-onset T1D, almost all of which (95%) had decreased expression (Fig. 3A and data S7). Basal acinar and other acinar subtypes showed down-regulation of numerous pathways in recent-onset T1D including those related to signaling, stimulus response, metabolism, and protein transport (Fig. 3A and table S9). In multiple ND AAB⁺, the high-enzyme acinar subtype showed significantly higher expression of antigen presentation, interferon signaling, and immune-related pathways, as well as increased activity of amino acid metabolism, which is necessary for enzyme production, carbohydrate and glucose metabolism, transcriptional activity, and respiration (Fig. 3J and table S9). We also observed down-regulation of genes in ductal cells in T1D associated with small molecule transport, stimulus response, cytokine signaling, and RNA processing but no evidence for changes in ND AAB⁺ (table S9).

Other cell types in islets and the surrounding microenvironment also had significant changes in activity across entire pathways during progression to T1D. In α cells, antigen presentation, interferon signaling, and other pathways were significantly increased in T1D with less pronounced effects for these pathways in multiple ND AAB⁺ and, in contrast to β cells, little change in single ND AAB⁺ (Fig. 3J and table S9). δ Cells showed more prominent changes in multiple ND AAB⁺, including significantly increased hypoxia and heat stress response and cell cycle-related pathways and decreased signaling pathways, as well as in single ND AAB+ (Fig. 3J and table S9). In endothelial cells, we observed increased interleukin-2 (IL-2) and JAK-STAT signaling as well as Stem Cell Factor (SCF)/ KIT signaling, which promotes angiogenesis (34, 35), in recentonset T1D (Fig. 3J and table S9). In activated stellate cells, there was decreased expression of translation and RNA processing in ND AAB⁺ and down-regulation of many pathways in recent-onset T1D (table S9). We observed few significant changes in gene or pathway activity in immune (T cell and macrophage) cells, although this could be due to the small number of cells profiled for these cell types.

Together, these results reveal key genes and pathways altered in pancreatic cell types in ND AAB⁺ and T1D donors with both shared

and distinct changes in ND AAB $^+$ compared to T1D, which in ND AAB $^+$ included antigen presentation, interferon signaling, ECM-related and stress response pathways in β cells, and metabolism and immune signaling in acinar cells.

Changes in the pancreatic cell type-specific epigenome in T1D progression

We next examined to what extent altered gene and pathway activity in pancreatic cell types in T1D progression is driven by changes in the epigenome using snATAC-seq profiles from 30 ND, ND AAB⁺, and T1D donors from nPOD. First, we identified cREs in each cell type with altered activity in T1D progression using a linear mixed model to account for pseudo-replication (see Materials and Methods). We observed significant changes (FDR < 0.1) in cRE activity in ND AAB⁺ (single and multiple) and T1D for most pancreatic cell types (data S8). β Cell cREs with increased activity in recent-onset T1D were significantly enriched (FDR < 0.1) for sequence motifs of steroid hormone receptors (NC3C1 and NR3C2), NF-Y (NFYA, NFYB, and NFYC), interferon response factors (IRF2 and IRF7), and stress-response TFs (ATF4, STAT1, and CEBPG) among others (Fig. 4A and table S10). Conversely, cREs with decreased activity in T1D were significantly enriched for sequence motifs of TFs involved in core β cell functions, such as HNF1 and RFX, with many β cell identity TFs (NKX6.1 and PDX1) and other TF families including FOXA and MEF showing more nominal enrichment (Fig. 4A and table S10). We also identified sequence motifs enriched in β cell cREs altered in ND AAB⁺, including IRF, TCF, and STAT TF motifs in cREs with increased activity and MEF, RFX, and NFAT TFs in cREs with decreased activity, although other T1D-associated motifs such as HNF1 showed no change in ND AAB⁺ (Fig. 4A and table S10). Sequence motifs were also enriched cREs altered in T1D progression for other pancreatic cell types, such as MEF and RFX TF motifs in α cells, RUNX TF motifs in activated stellate cells, STAT TF motifs in endothelial cells, and FOS/JUN motifs in ductal cells.

We determined next whether TF motifs enriched in T1Dassociated cREs in pancreatic cell types had broader, genome-wide changes in activity in T1D progression by modeling sequence motif accessibility across individual cells using chromVAR (see Materials and Methods) (26). In β cells, we observed consistent changes in the genome-wide accessibility of specific sequence motifs in T1D progression, including increasing accessibility of IRF motifs and decreasing accessibility of RFX, FOXA, and MEF motifs from ND AAB⁺ to T1D states (Fig. 4B and table S11). In other cases, sequence motifs had different patterns in ND AAB+ and T1D, such as decreased accessibility of HNF1 and increased accessibility of PARrelated and hormone receptor TFs in T1D only and opposed accessibility of SIX TFs in ND AAB⁺ and T1D. While α cells showed similar increases in accessibility of hormone receptor, stress response, and PAR-related TFs in T1D progression as in β cells, there were also several marked differences such as increased accessibility of MEF and RFX motifs in ND AAB⁺ and recent-onset T1D, respectively (Fig. 4B and table S11).

We used TF GRNs to determine which TFs drive changes in pathway activity in T1D progression. In β cells, pathways altered in ND AAB $^+$ and T1D had highly specific links to TF GRNs, suggesting key regulators of pathway activity in T1D progression (Fig. 4C and data S6). For example, pathways up-regulated in β cells in T1D and ND AAB $^+$ such as interferon signaling were linked to GRNs for IRF TF motifs, and antigen processing and presentation were linked

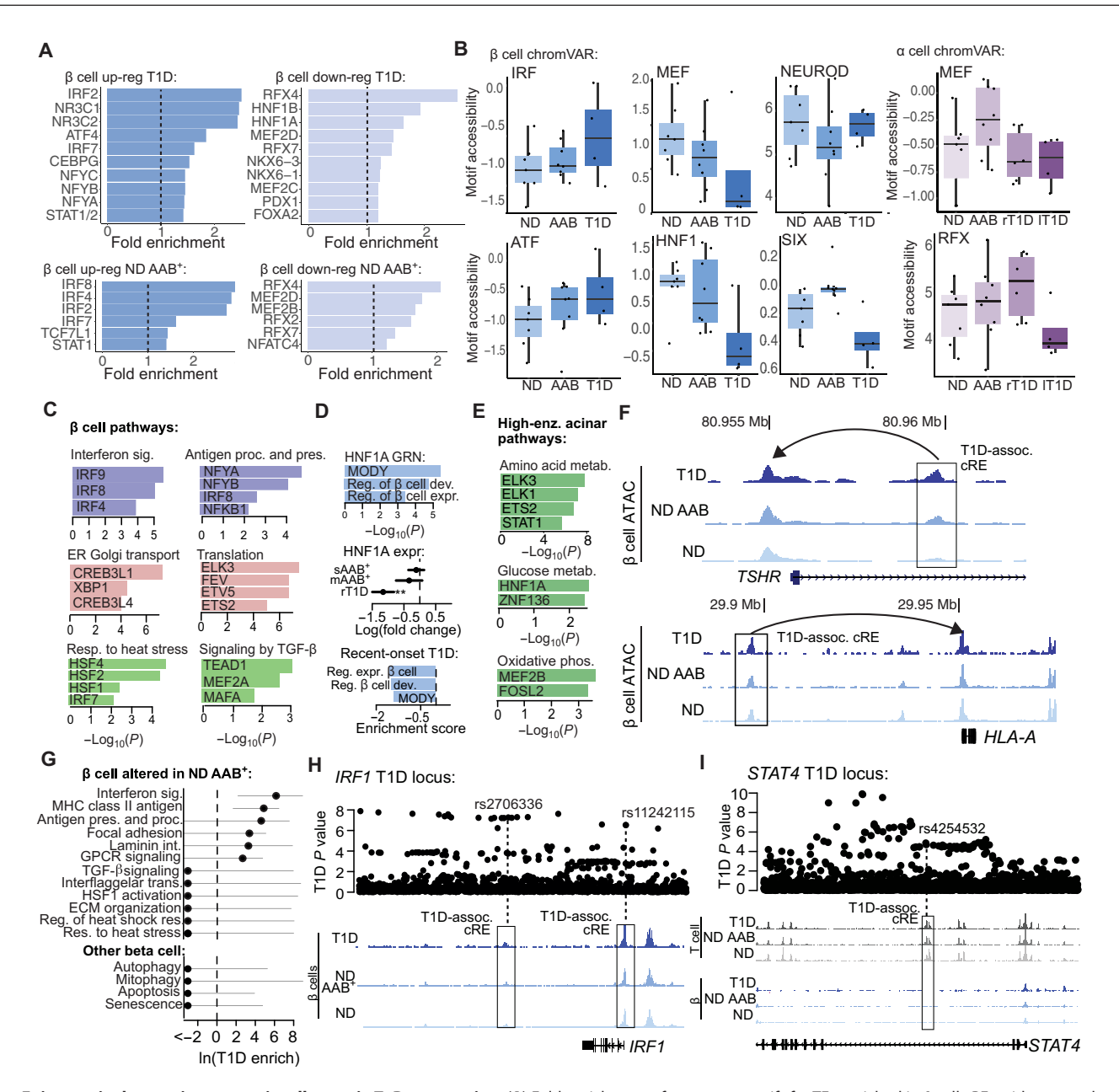


Fig. 4. Epigenomic changes in pancreatic cell types in T1D progression. (**A**) Fold enrichment of sequence motifs for TFs enriched in β cell cREs with up-regulated or down-regulated activity in (top) recent-onset T1D or (bottom) ND AAB⁺ (both single and multiple) using snATAC-seq from 30 donors (nPOD). (**B**) Box plots showing donor-level genome-wide accessibility of selected TF motifs in β cells (left) and α cells (right) from chromVAR across nondiabetes (ND), ND AAB⁺, and recent-onset T1D (T1D). (**C**) TF GRNs enriched for overlap with genes in biological pathways in β cells altered in T1D progression. (**D**) Biological pathways in β cells enriched for overlap with the HNF1A GRN (top). β Cell expression of HNF1A in T1D progression, values represent log fold change and error bars are SE (middle). β Cell activity of biological pathways linked to the HNF1A GRN in T1D progression (bottom). (**E**) TF GRNs enriched for overlap with genes in biological pathways in acinar cells altered in T1D progression. (**F**) Genome browser views of the *TSHR* (top) and *HLA-A* (bottom) loci where β cell cREs with altered activity in T1D were linked to genes with concordant changes in expression in T1D. (**G**) Genome-wide enrichment of T1D-associated variants in β cell cREs linked to pathways with altered expression in ND AAB⁺. Values represent log enrichment from fgwas, and error bars are 95% confidence interval. (**H**) Genome browser view of T1D-associated variants and β cell accessible chromatin in ND, ND AAB⁺, and T1D at the *IRF1* locus, where candidate T1D variant overlaps a β cell cRE with altered activity in T1D progression. (**I**) Genome browser view of T1D-associated variants and both β cell and T cell accessible chromatin in ND, ND AAB⁺, and T1D at the *STAT4* locus. Candidate T1D variants at this locus overlap T cell cREs.

to NFY, IRF, and nuclear factor κB (NF- κB) TF GRNs, while down-regulated pathways in T1D such as ER and Golgi-related processes were linked to CREB3L1, XBP1, and other TF motifs (Fig. 4C). We also identified TF GRNs linked to pathways altered specifically in ND AAB⁺, such as heat stress–related pathways and heat shock factor (HSF) TF GRNs, ECM-related pathways and ETS, ELK and ELF TFs, and GPCR signaling pathways and RFX and FOXA GRNs (Fig. 4C and data S6). While we observed a strong change in HNF1 motif accessibility, as well as HNF1A expression, in β cells in T1D (Fig. 4, B and D), no pathways linked to the HNF1 GRN had a significant change in expression in T1D. However, there was a more nominal change in β cell development and function pathways linked to the HNF1 GRN in T1D (Fig. 4D), supporting that reduced HNF1 activity likely underlies altered β cell function in T1D, as has been shown in the context of type 2 diabetes (36).

Similarly, in other pancreatic cell types, TF GRNs were linked to pathways with altered activity in ND AAB⁺ or T1D. For example, in enzyme-high acinar cells, metabolic pathways altered in ND AAB⁺ were linked to GRNs for specific TFs such as glucose metabolism and HNF1, amino acid metabolism and STAT1, and oxidative phosphorylation and MEF and FOS TF GRNs (Fig. 4E and data S6). In activated stellate cells, fibrin-related pathways up-regulated in ND AAB⁺ were significantly linked to ELK, HOX, CEBP, and other TF GRNs. In endothelial cells, IL-2 and JAK-STAT signaling pathways up-regulated in T1D were strongly linked to NF-κB (REL and RELA) and IRF TF GRNs, and SCF/KIT signaling was also linked to HOX family TF GRNs, among others. We further explored changes in TF activity inferred from spatial gene expression profiles of TF GRNs across cell types, which revealed increased activity of immune regulation, inflammation and signaling TFs (e.g., STAT3, RBPJ, FOSL2, and JUND), and reduced activity of endocrine-related TFs (e.g., PAX6, GLI3, MAFA, INSM1, and NEUROD1), in T1D compared to nondisease (fig. S12).

We next annotated specific β cell cREs altered in T1D progression with putative target genes and assessed changes in regulatory programs at specific loci. There were 114 β cell cREs with altered activity in T1D progression linked to genes with significant changes in expression. For example, a β cell cRE on chromosome 14 in the first intron of TSHR had increased accessibility in recent-onset T1D and was linked to TSHR, which had among the largest increases in expression in recent-onset T1D (Fig. 4F). We identified similar cREs up-regulated in recent-onset T1D linked to genes with highly up-regulated expression including HLA-A (Fig. 4F), as well as CD74, GAD1, IL15, and STAT1/4. In other cases, we observed epigenomic changes in β cells that may precede changes in expression of cognate target genes. For example, a cRE upstream of IAPP had reduced accessibility in early T1D, although IAPP itself only had a significant decrease in expression in longer-duration T1D.

Given pathways and transcriptional regulators with altered cell type activity in T1D progression, we determined whether any changes before T1D onset showed evidence for a role in genetic risk of T1D. We tested for enrichment of cREs linked to genes in each pathway for T1D-associated variants genome-wide (excluding the MHC locus) using fgwas (see Materials and Methods) (5, 37). In β cells, several pathways altered in ND AAB $^+$ were enriched for T1D-associated variants including antigen processing and presentation (log enrich = 4.48), class II MHC antigen presentation (log enrich = 4.74), and interferon signaling (log enrich = 6.00) as well as several extracellular interaction-related processes (focal adhesion

and laminin interactions) and GPCR signaling (Fig. 4G). By comparison, multiple other pathways previously implicated in driving T1D risk in β cells, such as apoptosis, autophagy, mitophagy, and senescence, showed limited to no enrichment (Fig. 4G). Among other cell types, we found evidence for enrichment of immune, metabolism, and transcription-related pathways in high-enzyme as well as basal acinar cells (fig. S13).

We further identified specific T1D risk loci that may alter regulatory activity of disease-enriched pathways in key cell types such as β cells, T cells, and other immune populations and exocrine cells during T1D progression. We identified candidate causal variants at known T1D loci by overlapping cREs altered in T1D progression with published fine-mapping data (5). In β cells, multiple candidate causal variants at the *IRF1* locus overlapped cREs with increased activity in T1D including at the promoter and downstream of IRF1 (Fig. 4H and table S12). There was increased β cell expression of IRF1 through stages of T1D progression, and *IRF1* is a driver of β cell interferon responses, which is a pathway broadly enriched for T1D-associated sponses, which is a pathway broadly enriched for T1D-associated riants (Fig. 4H). Conversely, at the *STAT4* locus, we identified cREs th increased activity in β cells as well as T cells, although candidate usal variants for T1D at the *STAT4* locus only overlapped cREs acte in T cells (Fig. 4I). This finding supports that while increased *AT4* activity in β cells is observed in T1D, the *STAT4* locus more ely affects T1D risk through altered T cell function.

Proinflammatory cytokine exposure has been used as a model to add genetic risk of T1D in β cells (12, 38) but the cytost to which variants (Fig. 4H). Conversely, at the STAT4 locus, we identified cREs with increased activity in β cells as well as T cells, although candidate causal variants for T1D at the STAT4 locus only overlapped cREs active in T cells (Fig. 4I). This finding supports that while increased STAT4 activity in β cells is observed in T1D, the STAT4 locus more likely affects T1D risk through altered T cell function.

study genetic risk of T1D in β cells (18, 38), but the extent to which cytokine-induced changes in β cells captures transcriptional regulators and sites of T1D risk in actual T1D progression is not well established. Several TF motifs enriched in cytokine-responsive cCREs mirrored those enriched in cCREs up-regulated in T1D including IRF and STAT TFs, while other TFs such as steroid hormones may be more specific to T1D progression. We next compared the overlap of T1D risk loci with cCREs altered in T1D progression and cytokine-responsive cCREs from a prior study (38). Risk variants at a subset of T1D loci overlapped both sets of cCREs, including the IRF1 locus. These results suggest that cytokine exposure partially recapitulates epigenomic changes in β cells during T1D progression and may help model disease mechanisms at specific loci. Together, these results reveal transcriptional regulators and networks altered in T1D progression, including those regulating pathways that likely play a causal role in T1D such as antigen presentation, interferon signaling, and extracellular interactions in β cells.

Changes in pancreatic cell-cell signaling in T1D progression

External signaling between cell types is a key driver of changes in cell type–specific regulation and function, and therefore, we lastly identified cell-cell signaling interactions in the pancreas altered in T1D progression. We first inferred cell-cell interactions using snRNA-seq data for 32 nondiabetes, ND AAB⁺ (both single and multiple), and T1D donors in nPOD using 1939 ligand-receptor (LR) pairs in CellChat (see Materials and Methods) (39), which revealed 87,650 interactions significant (FDR < 0.1) in at least one condition (table S13). Grouping ligands into functional categories revealed classes of outgoing signals preferentially produced by each cell type; for example, hormones, neuropeptides, and cell adhesion molecules from endocrine cells and enzymes from exocrine cells (fig. S14 and table S14).

We identified cell-cell interactions with changes in activity in T1D progression using a permutation test and considered changes significant at FDR < 0.1 (see Materials and Methods). Overall, there

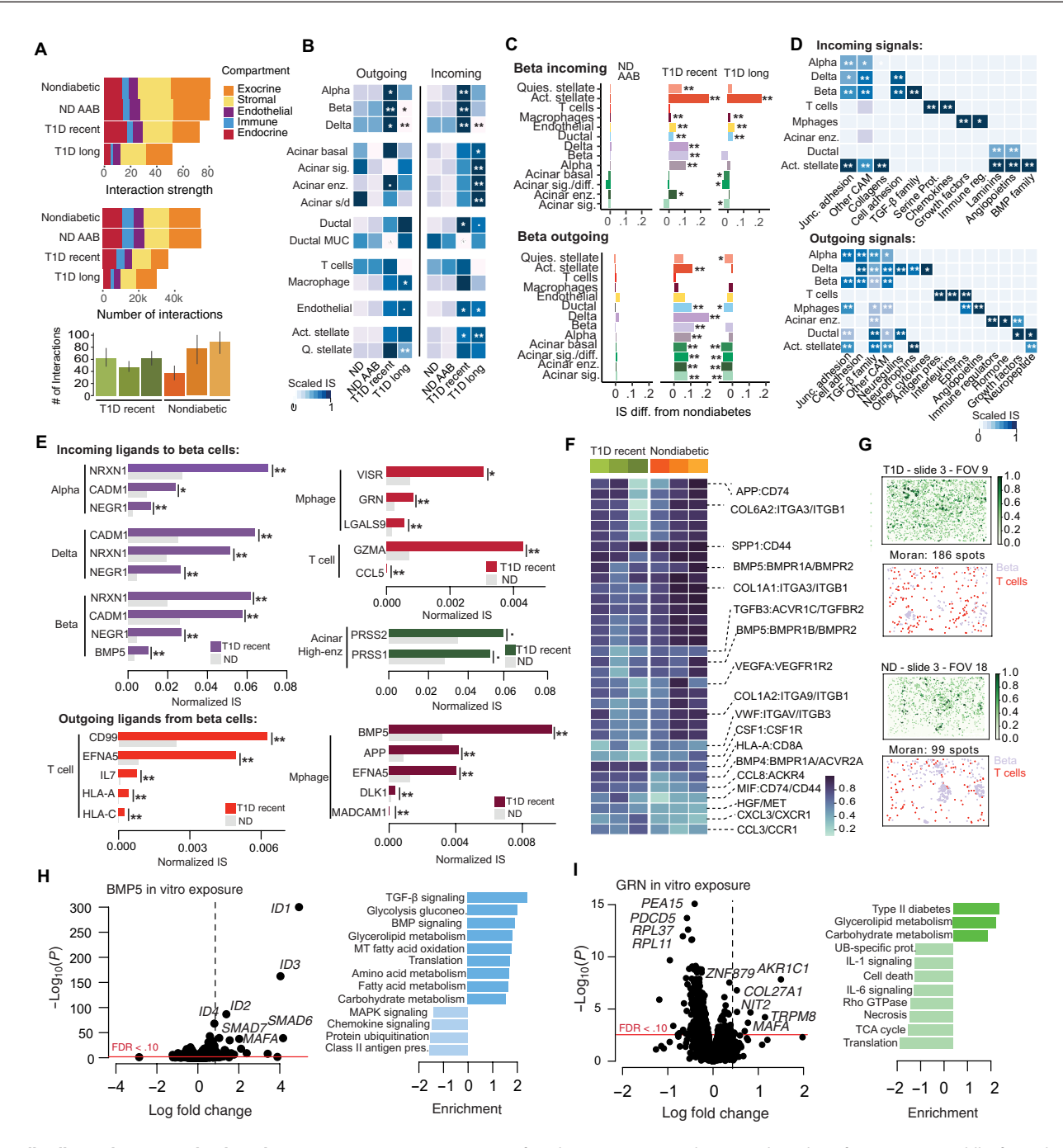


Fig. 5. Cell-cell signaling networks altered in T1D progression. (**A**) Summary of total interaction strength (top) and number of interactions (middle) for each pancreatic lineage in nondiabetes, ND AAB⁺ (both single and multiple), recent-onset T1D, and long-standing T1D using snRNA-seq from 32 donors (nPOD). Bar plot showing the number of LR interactions per donor FOV in spatial slides, and error bars are SE (bottom). (**B**) Heatmap showing normalized interaction strength of signals for each cell type among donors which were nondiabetes, ND AAB⁺, recent-onset T1D, and long-standing T1D. Stars represent significance of the difference in interaction strength in each T1D state compared to nondiabetes. **FDR < 0.01 and *FDR < 0.05. (**C**) Difference in strength of interactions between β cells and other cell types and subtypes in ND AAB⁺, recent-onset T1D, and long-duration T1D. **FDR < 0.01 and *FDR < 0.05. (**D**) Interaction strength of signals for each cell type summarized by functional categories. **FDR < 0.01 and *FDR < 0.05. (**C**) Normalized interaction strength in recent-onset T1D and nondiabetes for ligands with significant change in signal involving β cells. **FDR < 0.01 and *FDR < 0.05. (**F**) Heatmap per donor showing the interaction score of the top LR interactions from a likelihood ratio test comparing ND and T1D donors. (**G**) Spatial plots of a representative FOV (T1D: top, ND: bottom) highlighting spots with an interaction between *HLA-C* and *CD8A* and the cell types where this interaction occurs. (**H**) Volcano plot showing genes with up- and down-regulated expression in EndoC-BH1 after BMP5 treatment (left). Pathways enriched in up- and down-regulated genes in BMP5 exposure (right). The experiment was performed using n = 6 biological replicates per treatment. MAPK, mitogenativated protein kinase. (**I**) Volcano plot showing genes with up- and down-regulated expression in EndoC-BH1 after progranulin (PGRN) treatment (left). Biological pathways enriched in genes with up- and down-regulated expr

was a reduction in the number and strength of interactions in recentonset and long-standing T1D compared to nondiabetes, which was largely driven by exocrine cells (Fig. 5A). In both ND AAB $^+$ and recent-onset T1D, there was increased strength of interactions involving endocrine cells and other cell types, although the total number of interactions was reduced (Fig. 5A). We further identified cell-cell interactions among cells in spatial niches and determined changes in T1D using spatial transcriptome profiles. We identified spatially coexpressed LR interactions by Moran's bivariant extension in SpatialDM (40) using LR pairs from CellChat (39). We compared the number of detected interactions considering each FOV as technical replicates of a donor and observed significant heterogeneity across donors and, like dispersed cell data, fewer interactions in T1D compared to ND donors (H statistic = 19.6, P = 0.0015) (Fig. 5A).

Among specific cell types, endocrine cells displayed significant increases in both outgoing and incoming signaling in recent-onset T1D (Fig. 5, B and C). We also observed significant increases in incoming signaling to endothelial, ductal, and activated stellate cells, as well as nominal changes in basal and high-enzyme acinar, immune, and stellate cells, in recent-onset T1D. Summarizing signaling by functional category revealed broad classes of cell type-specific signals altered in T1D; for example, β and other endocrine cells had increased signaling from cell adhesion molecules, whereas T cells had increased antigen presentation and interleukin signaling (Fig. 5D). We further examined changes in signaling between specific pairs of cell types in T1D progression (table S15). Significant changes (FDR < 0.1) in recentonset T1D included increased incoming and outgoing signaling involving β cells, including between β cells themselves (Fig. 5C), as well as increased signaling for α cells, outgoing signaling from highenzyme acinar cells, and incoming signaling to endothelial cells.

Given the importance of external signaling to β cells in T1D, we focused specifically on signals involving β cells. In recent-onset T1D, autocrine/paracrine signals incoming to β cells with significant changes in activity included cell adhesion molecules NRXN1, CADM1, and NEGR1 from all endocrine cell types and the secreted factor *BMP5* from β cells (Fig. 5E). In addition, high-enzyme acinar cells had increased signaling of trypsinogen (Fig. 5E), and stellate cells had increased signaling of ECM and cell adhesion molecules to β cells. Among immune cells, signals with significant changes in signaling to β cells included GZMA and CCL5 from T cells and VSIR, PGRN, and LGALS9 from macrophages (Fig. 5E). In return, β cells had increased signaling of IL7 and MHC class I genes HLA-A and *HLA-C* to T cells, as well as increased signaling of *BMP5*, *EFNA5*, *DLK1*, and *ANGPTL2* to macrophages. Notably, multiple β-immune cell signals altered in a T1D map to T1D risk loci (e.g., DLK1, HLA-A, HLA-C, and IL7R) (5).

We next identified differential interactions (P < 0.05) in spatial profiles by performing a likelihood ratio test, which provided support for many T1D-associated interactions identified in dispersed cell data. For example, interactions involving HLA class I (e.g., HLA-C), APP, SPP1, and BMP5, as well as ECM-related interactions, were altered in T1D (Fig. 5, F and G). We also identified additional interactions enriched in T1D donors, for example, between migration inhibitory factor MIF and its transmembrane receptor CD74, consistent with previous studies (41), and involving several chemokines. Next, we identified spatially coexpressed LR pairs using the Moran's I score in Liana+ (32). We obtained the top interactions associated with each niche using non-negative matrix factorization (see Materials and Methods). In T1D, an interaction between APP

and *CD74* was enriched in the endocrine niche, where APP is involved in inflammation and could promote immune responses in T1D (fig. S15). Conversely, interactions involving *INS*, *IGF1R*, *INSR*, and *CALM1*, among others, were enriched in the endocrine niche from nondisease donors (fig. S15).

Several ligands that signal to β cells in T1D progression including BMP5 and PGRN have not been previously implicated in T1D, and cellular responses to these ligands may contribute to changes in gene activity observed in β cells in T1D. We thus determined the effects of in vitro exposure to these ligands on gene expression using the β cell model EndoC-BH1. Exposing β cells to BMP5 in culture revealed 1926 genes with significant change (FDR < 0.1) in expression, where the most up-regulated genes were *ID1-4* and *SMAD6-7*, known targets of BMP that regulate proliferation and differentiation, and the β cell identity gene MAFA (Fig. 5H and table S16). More broadly, BMP5 exposure up-regulated pathways (FDR < 0.1) related to TGF-β signaling, glycolysis, secretion, and lipid metabolism and down-regulated pathways such as antigen presentation and chemokine signaling (Fig. 5H). Second, PGRN encodes secreted proteins produced by macrophages and ductal cells. Upon exposure to granulin, 491 genes had a significant change (FDR < 0.1) in expression including up-regulation of β cell function and insulin secretion genes MAFA, ISL1, SOX4, CRY2, and down-regulation of apoptosis-related genes PEA15, PDCD5, and CCAR1 (Fig. 5I and table S17). More broadly, granulin up-regulated cholesterol and glycerolipid metabolism and down-regulated interleukin signaling and inflammation, transcription and translation, and cell death. Overall, these results support that both BMP5 and PGRN suppress pathways up-regulated in β cells in T1D and therefore may play a protective role in β cells during T1D progression. These results together reveal broad changes in predicted cell-cell signaling in T1D progression most prominently among endocrine cells and niches but also involving other cell types, including signals altered in T1D that modulate T1D-relevant regulatory programs in β cells.

DISCUSSION

Single-cell and spatial profiling of human pancreas donors revealed extensive changes in the abundance, regulation, and signaling of specific cell types in T1D progression, including processes that play a likely causal role in driving disease. In β cells, class I and class II MHC antigen presentation and interferon signaling pathways, TF regulators of these pathways, and cREs linked to genes in these pathways all had up-regulated activity in recent-onset T1D and ND AAB⁺. Antigen presentation was altered as early as single ND AAB⁺ donors, suggesting that aberrant antigen presentation in β cells may be an initial triggering event in T1D. A larger proportion of β cells from ND AAB+ and T1D donors expressed antigen presentation pathways, although whether subsets of these cells drive initiation or exacerbation of immune responses requires further investigation. Antigen presentation and interferon signaling pathways in β cells were broadly enriched for T1D-associated variants, and specific risk loci for T1D were linked to key genes in these pathways such as *IRF1*. In contrast, we found limited evidence that pathways directly related to apoptosis, as well as other processes implicated in T1D in β cells such as autophagy, senescence, and mitophagy, harbor T1D risk and are thus more likely consequences of disease. It has been long hypothesized that β cells affect genetic risk of T1D through increased cell death (41–47). Our results support that β cells may

primarily contribute to T1D risk via the initiation or exacerbation of immune responses, which necessitates different cellular models and phenotypic readouts to understand their role in disease.

In addition to shared pathways, gene activity in β cells and other pancreatic cell types had distinct changes in ND AAB⁺ compared to recent-onset T1D, revealing that genomic profiles before T1D onset are only partially intermediate to those in T1D. In addition, the lack of individual genes with highly significant changes expression in ND AAB+ suggests that changes at these stages are likely more subtle, in contrast to previous reports (4). Several pathways in β cells were altered specifically in single and multiple ND AAB⁺ such as heat shock response and ECM organization. Heat shock responses are activated by a variety of stressors, promote antigen presentation in β cells, and can act as chaperones for antigens and thus may plausibly contribute to the initiation of autoimmunity (48, 49). The breakdown of ECM is also an important process in T1D, as both a precursor to immune invasion and by affecting intrinsic β cell function (50). We observed a similar pattern of both shared and distinct changes in the epigenome of β cells in ND AAB⁺ compared to T1D, including increased NEUROD1 activity and decreased SIX TF activity. There were also shared and distinct features in T1D based on the duration of disease; for example, a more pronounced reduction in β cell function in long-standing T1D.

In contrast to β cells, changes in pathway activity in α cells were largely restricted to multiple ND AAB+ and T1D, including antigen presentation and interferon response pathways and transcriptional regulators of these pathways. This supports that immune responses are more pronounced within β cells compared to α cells particularly in the early stages of T1D, which may reflect differences in immune targeting as well as the intrinsic properties of each cell type. The latter is supported by in vitro studies showing pronounced responses of β cells to external stressors (18). A previous study revealed changes in α cell function and gene expression in single ND AAB+ using data from HPAP (51), although there were overall few genes with altered expression which supports our findings that genomic changes in α cells before T1D are likely subtle. In addition, several TF families such as RFX and MEF2 had different patterns of accessibility between α cells and β cells in T1D, further highlighting the unique responses of each cell type to disease. Conversely to α cells, δ cells had altered activity of multiple stress and inflammatory response pathways both in single and multiple ND AAB⁺, as well as decreased abundance in T1D, suggesting that they may play an as-of-yet unappreciated role in T1D progression.

Given that we profiled pancreatic tissue samples and not purified islets, our study was uniquely placed to reveal changes in the exocrine pancreas compared to previous single-cell studies (4, 15). We identified multiple clusters of acinar and ductal cell types which had distinct genomic profiles and may represent heterogeneous subtypes of these cell types. In acinar cells, subclusters were broadly related to enzyme production and signaling responses, and previous reports highlighted similar heterogeneity in secretory and idling acinar cells (52). Similar hormone-producing and signaling states have been reported in endocrine cells (53) and thus may represent a common property of secretory cells. Resolving exocrine subclusters revealed genomic changes within specific exocrine subtypes in T1D. Enzyme-high acinar and MUC5B⁺ ductal cells were more abundant in ND AAB⁺ donors, and acinar subtypes had altered immune signaling, metabolism, and transcriptional pathways, as well

as increased signaling to β cells, in T1D progression. Specific pathways within acinar cells altered in T1D progression also harbored T1D-associated variants, further supporting a role for exocrine pancreas in T1D risk (4, 5) and providing new in-roads to determine how cellular processes in acinar cells contribute causally to T1D.

Signaling relationships between pancreatic cell types revealed incoming and outgoing external signals during progression to T1D. Cell-cell signaling between immune and β cells highlighted known signals in T1D (54, 55), as well as potential mechanisms of genes implicated in T1D risk such as *DLK1* and *IL7* (5). Additional signals incoming to β cells in T1D such as BMP5 and PGRN have no prior known role in disease. BMP5 has increased autocrine/paracrine signaling in T1D and in vitro suppressed antigen presentation- and chemokine-related genes and enhanced expression of several genes linked to $\boldsymbol{\beta}$ cell proliferation and function. Other BMP proteins have been shown to both enhance and inhibit β cell function, maturity, and proliferation (56-58), where the direction of effect depends on the level of BMP signaling. PGRN suppresses class I MHC expression and T cell infiltration of ductal adenocarcinoma cells in the context of pancreatic cancer and has been shown to promote proliferation in mouse models of β cells (59, 60). Signaling pathways altered in T1D, particularly those involved in T1D risk, may represent therapeutic areas for preserving β cell function to prevent or reverse T1D.

There were several limitations of the data and analyses in our study to highlight. Current single-cell and spatial assays provide sparse profiles per cell which can affect downstream analyses. For example, although we used data integration methods designed to overcome sparsity in spatial data (21), there are still challenges in annotating cell types and subtypes among cells with sparse profiles. In addition, analyses such as differential expression, TF activity, and cell-cell communication likely underrepresent true biological signals that are lowly expressed and have more limited detection in single-cell and spatial assays. The data from single-cell and spatial assays also represent a limited sample of the whole pancreas. For example, our single-cell assays profiled the head of the pancreas, and whether cell type-specific changes in T1D in this region reflect those in the body and tail is unknown. Similarly, spatial assays profiled FOV selected on the basis of specific criteria which limited our ability to define changes in T1D more broadly across the pancreas. Overcoming these limitations with current technology could consist of repeated assays per donor covering many different regions and FOV. Last, cell-cell interactions in our study represent predictions based on gene expression, which may not necessarily reflect ligand and receptor protein abundance nor capture direct LR interactions, and additional experiments are needed to validate these interactions.

Last, one key area for future studies to address is the still relatively limited profiling of donors across all dimensions of T1D pathogenesis and progression. For example, we profiled few donors from nPOD that were single ND AAB⁺, which prohibited understanding changes in nonendocrine cells in the earliest stages of disease initiation. In addition, while we grouped ND donors by the number of autoantibodies, there is further granularity in how T1D stages can be defined. For example, stage 2 of T1D is marked by both multiple autoantibody positivity and reduced β cell function (61), and refined characterization of T1D stages may help reveal drivers of dysglycemia in T1D progression. The extent of differences in genomic profiles of heterogeneous subgroups of T1D, for example, based on age of onset, HLA background, or other variables (62–64), is also largely unknown. Continued collection of single-cell and

spatial data from much larger sample sizes will be instrumental in enabling all these analyses. Last, studies pairing pancreas data with other T1D-relevant tissues from matched donors, for example, pancreatic lymph nodes, will help understand immune infiltration and cross-tissue signaling in driving T1D in the pancreas.

In summary, our study revealed gene regulatory changes in pancreatic cell types in T1D progression and highlighted pathways, regulatory networks, and signals that may play a causal role in T1D; efforts that inform both new directions for mechanistic studies and targets for therapies to prevent or reverse T1D. We provide these data and maps in visualization tools at http://t1d-pancreas.isletgenomics. org to further enhance their utility to the research community. More broadly, our study highlights the utility of single-cell multiomic and spatial analysis to reveal insight into cellular processes underlying progression to complex disease.

MATERIALS AND METHODS

Sample selection

Whole pancreas tissue was obtained from the nPOD biorepository according to federal guidelines with informed consent obtained from each donor's legal representative. Studies were considered exempt and approved by the Institutional Review Board of the University of California San Diego. We selected 7 T1D donors with more recent onset (<1 year from diagnosis) and 5 T1D donors with longer duration (>5 years from diagnosis), along with 11 age- and sexmatched ND individuals. We also selected nine ND donors with T1D autoantibodies (ND TD AAB⁺), most of which had multiple antibodies although one donor was single GAD⁺. In total, 32 donors were obtained for genomic profiling. For all 32 donors, frozen tissue samples were obtained from head of the pancreas (table S1).

Single-cell assays

Tissue homogenization

For each sample, we homogenized roughly 40 mg of flash-frozen pancreas tissue using mortar and pestle on liquid nitrogen, and ground tissue was used as input for the different single-nucleus assays.

Generation of snATAC-seq data

Ground pancreas tissue was resuspended in 1 ml of nuclei permeabilization buffer [10 mM tris-HCl (pH 7.5), 10 mM NaCl, 3 mM MgCl₂, 0.1% Tween 20 (Sigma-Aldrich), 0.1% IGEPAL-CA630 (Sigma-Aldrich), 0.01% digitonin (Promega), and 1% fatty acid-free bovine serum albumin (BSA) (Proliant, 68700) in molecular biology–grade water]. Nuclei suspension was filtered with a 30-µm filter (CellTrics, Sysmex) and then incubated for 5 min at 4°C on a rotator. Nuclei were pelleted with a swinging bucket centrifuge (500g, 5 min, 4°C; Eppendorf, 5920 R) and washed with 1 ml of wash buffer [10 mM tris-HCl (pH 7.5), 10 mM NaCl, 3 mM MgCl₂, 0.1% Tween 20, and 1% BSA (Proliant, 68700) in molecular biology-grade water]. Nuclei were pelleted and resuspended in 10 μl of 1× nuclei buffer (10x Genomics). Nuclei were counted using a hemocytometer, and 15,360 nuclei were used for tagmentation. snATAC-seq libraries were generated using the Chromium Single Cell ATAC Library & Gel Bead Kit v1.1 (10x Genomics, 1000175), Chromium Chip H Single Cell ATAC Kit (10x Genomics, 1000161), and indexes (Single Index Kit N Set A, 1000212) following the manufacturer's instructions. Final libraries were quantified using a Qubit fluorometer (Life Technologies), and the nucleosomal pattern was verified using a TapeStation (High Sensitivity D1000, Agilent). Libraries were sequenced on

NextSeq 500, HiSeq 4000, and NovaSeq 6000 sequencers (Illumina) with the following read lengths (Read1 + Index1 + Index2 + Read2): 50 + 8 + 16 + 50. Libraries were sequenced to an average depth of 333M reads (table S1).

Generation of snRNA-seq data

Ground pancreas tissue was suspended in 500 µl of nuclei buffer: 0.1% Triton X-100 (Sigma-Aldrich, T8787), 1× EDTA free protease inhibitor (Roche or Pierce), 1 mM dithiothreitol (DTT), and ribonuclease (RNase) inhibitor (0.2 U/µl; Promega, N211B), and 2% BSA (Sigma-Aldrich, SRE0036) in phosphate-buffered saline (PBS). Sample was incubated on a rotator for 5 min at 4°C and then pelleted with a swinging bucket centrifuge (500g, 5 min, 4°C; 5920 R, Eppendorf). The supernatant was removed, and the pellet was resuspended in 400 µl of sort buffer [1 mM EDTA and RNase inhibitor (0.2 U/µl) in 2% BSA (Sigma-Aldrich, SRE0036) in PBS] and stained with DRAQ7 (1:100; Cell Signaling Technology, 7406). A total of 75,000 nuclei were sorted using an SH800 sorter (Sony) into 50 μl of collection buffer [RNase inhibitor (1 U/μl) and 5% BSA (Sigma-Aldrich, SRE0036) in PBS]. Sorted nuclei were then centrifuged at 1000g for 15 min (Eppendorf, 5920R; 4°C, ramp speed of 3/3), and the supernatant was removed. Nuclei were resuspended in 18 to 25 μl of reaction buffer [RNase inhibitor (0.2 U/ $\mu l)$ and 1%BSA (Sigma-Aldrich, SRE0036) in PBS] and counted using a hemocytometer. A total of 16,500 nuclei were loaded onto a Chromium controller (10x Genomics). Libraries were generated using the 10x Genomics, Chromium Next GEM Single Cell 3' GEM, Library & Gel Bead Kit v3.1 (10x Genomics, 1000121), Chromium Next GEM Chip G Single Cell Kit (10x Genomics, 1000120), and indexes (Single Index Kit T Set A, 10x Genomics, 1000213 or Dual Index Kit TT Set A, 10x Genomics, 1000215) according to the manufacturer's specifications. cDNA was amplified for 12 polymerase chain reaction (PCR) cycles. SPRISelect reagent (Beckman Coulter) was used for size selection and cleanup steps. Final library concentration was assessed by the Qubit dsDNA HS Assay Kit (Thermo Fisher Scientific), and fragment size was checked using a TapeStation (High Sensitivity D1000, Agilent). Libraries were sequenced using a NextSeq 500 and a Novaseq6000 (Illumina) with the following read lengths (Read1 + Index1 + Index2 + Read2): 28 + 8 + 0 + 90 (single index) or 28 + 10 + 10 + 90 (dual index). Libraries were sequenced to an average depth of 206M reads and captured 1580 genes per nucleus (table S1).

Generation of joint single-nucleus RNA and ATAC-seq data (Multiome)

Ground tissue was resuspended in 1 ml of wash buffer [10 mM tris-HCl (pH 7.4), 10 mM NaCl, 3 mM MgCl₂, 0.1% Tween 20 (Sigma-Aldrich), 1% fatty acid-free BSA (Proliant, 68700), 1 mM DTT (Sigma-Aldrich), 1× protease inhibitors (Thermo Fisher Scientific, PIA32965), and RNasin (1 U μl⁻¹; Promega, N2515) in molecular biology-grade water]. Nuclei suspension was filtered with a 30-µm filter (CellTrics, Sysmex) and pelleted with a swinging bucket centrifuge (500g, 5 min, 4°C; Eppendorf, 5920 R). Nuclei were resuspended in 400 μ l of sort buffer [1% fatty acid–free BSA, 1× protease inhibitors (Thermo Fisher Scientific, PIA32965), and RNasin (1 U μl⁻¹; Promega, N2515) in PBS and stained with 7-aminoactinomycin D (1 µM; Thermo Fisher Scientific, A1310). A total of 120,000 nuclei were sorted using an SH800 sorter (Sony) into 87.5 µl of collection buffer [RNasin (1 U μl⁻¹; Promega, N2515) and 5% fatty acid-free BSA (Proliant, 68700) in PBS]. Nuclei suspension was mixed in a ratio of 4:1 with 5× permeabilization buffer [50 mM tris-HCl

(pH 7.4), 50 mM NaCl, 15 mM MgCl₂, 0.5% Tween 20 (Sigma-Aldrich), 0.5% IGEPAL-CA630 (Sigma-Aldrich), 0.05% digitonin (Promega), 5% fatty acid-free BSA (Proliant, 68700), 5 mM DTT (Sigma-Aldrich), 5× protease inhibitors (Thermo Fisher Scientific, PIA32965), and RNasin (1 U μl⁻¹; Promega, N2515) in molecular biology-grade water] and incubated on ice for 1 min before pelleting with a swinging bucket centrifuge (500g, 5 min, 4°C; Eppendorf, 5920 R). The supernatant was gently removed, and ~10 μl was left behind to increase nuclei recovery. A total of 650 µl of wash buffer [10 mM tris-HCl (pH 7.4), 10 mM NaCl, 3 mM MgCl₂, 0.1% Tween 20 (Sigma-Aldrich), 1% fatty acid-free BSA (Proliant, 68700), 1 mM DTT (Sigma-Aldrich), 1× protease inhibitors (Thermo Fisher Scientific, PIA32965), and RNasin (1 U μ l⁻¹; Promega, N2515) in molecular biology-grade water] was added with minimal disturbance of the pellet, and samples were centrifuged again with a swinging bucket centrifuge (500g, 5 min, 4°C; Eppendorf, 5920 R). The supernatant was gently removed without disturbing the pellet, leaving ~2 to 3 μl behind. Approximately 7 to 10 μl of 1× nuclei buffer (10x Genomics) were added, and nuclei were gently resuspended. Nuclei were counted using a hemocytometer, and 18,300 nuclei were used as input for tagmentation. Single-cell multiome ATAC and gene expression libraries were generated following the manufacturer's instructions (Chromium Next GEM Single Cell Multiome ATAC + Gene Expression Reagent Bundle, 10x Genomics, 1000283; Chromium Next GEM Chip J Single Cell Kit, 10x Genomics, 1000234; Dual Index Kit TT Set A, 10x Genomics, 1000215; Single Index Kit N Set A, 10x Genomics, 1000212) with the following PCR cycles: 7 cycles for preamplification, 8 cycles for ATAC index PCR, 7 cycles for cDNA amplification, and 12 cycles for RNA index PCR. Final libraries were quantified using a Qubit fluorometer (Life Technologies), and the size distribution was checked using a TapeStation (High Sensitivity D1000, Agilent). Libraries were sequenced on NextSeq 500 and NovaSeq 6000 sequencers (Illumina) with the following read lengths (Read1 + Index1 + Index2 + Read2): ATAC (NovaSeq 6000), 50 + 8 + 24 + 50; ATAC (NextSeq 500 with custom recipe), 50 + 8 + 16 + 50; RNA (NextSeq 500, NovaSeq 6000), 28 + 10 + 10 + 90. Libraries were sequenced to an average depth of 104M reads for RNA-seq and 247M reads for ATAC-seq and captured 1789 genes per nucleus (table S1).

Quality control and filtering

Single nuclei ATAC data were processed and aligned to reference genome hg38, and duplicate reads were removed using CellRanger ATAC (v1.1.0). Chromatin accessibility for each sample was quantified in 5-kb genome windows as previously described (53). Nuclei with less than 1000 unique ATAC-seq fragments were removed. Initial quality control was performed to retain cells in each sample using the following metrics unique usable reads > 5000, fraction promoters used > 0.01, and transcription start site (TSS enrichment) (TSSe) > 0.3 using scanPy v1.8.0. Doublets were removed using Amulet v1.0 per sample (65). After quality control, snATAC-seq profiles from two donors (6366 and 6459) were excluded from further analysis due to low barcode numbers and poor clustering.

Single-nuclei RNA samples were processed using CellRanger (v6.0.1) with reference genome hg38 (66). Individual samples were processed for quality initially by removing nuclei with less than 500 expressed genes. Doublets were detected for each sample using DoubletFinder (v2.0.3) using an expected doublet rate of 4% for all samples (67). In effort to reduce ambient RNA contamination

largely driven by acinar cells, we used SoupX (v1.6.2) and selected acinar marker genes, *REG1A* and *PRSS1*, to estimate contamination rates (68). Gene expression count matrices were then corrected for this predicted contamination, and these correct counts were used for both clustering and downstream analysis.

Paired multiome data were processed and aligned, and multiplet reads were removed using cellranger arc (v2.0.0) with the reference genome hg38. Individual sample quality control was done using both modalities to remove low-quality nuclei without a minimum of 500 expressed genes and 1000 ATAC-seq fragments. Ambient RNA contamination was removed using SoupX (v1.6.2) using the same parameters as previously described. Doublets were detected and removed for both modalities using DoubletFinder (v2.0.3) and Amulet (v1.0), with the same parameters as above for single modality data (65, 67).

Generation of spatial transcriptomic data

Pancreatic tissue from six nPOD organ donors—three with T1D (6228, 6247, and 6456) and three ND (6431, 6339, and 6229), matched by age and sex—was selected for spatial transcriptomic profiling on the CosMx platform (NanoString, Seattle, WA). For each donor, five consecutive Formalin-Fixed, Paraffin-Embedded (FFPE) tissue sections from the pancreatic body region were cut at a thickness of 4 μm. Sections #1, #2, #4, and #5 were mounted on the back of VWR Superfrost Plus Micro Slides, centered within the scanning area. After sectioning, the slides were air-dried overnight at room temperature, sealed, and immediately shipped with desiccant and ice packs to the NanoString facility (Seattle, Washington), where they were processed within 2 weeks of receipt. Section #3 was triple-stained for CD3, insulin, and glucagon using chromogen-based immunohistochemical staining using the Mach2 Double Stain 1/Mach2 Double Stain 2 HRP-AP Polymer Detection Kit according to the manufacturer's instructions (Biocare Medical, Pacheco, CA), and chromogens used included Betazoid Diaminobenzidine (DAB) (CD3), Warp Red (insulin), and Ferangi Blue (glucagon; all from Biocare Medical). Slides were then counterstained with hematoxylin. After staining, the slide was digitized at ×20 magnification using an Aperio CS2 slide scanner (Leica Biosystems Inc., Wetzlar, Germany), and this image served as a reference for FOV selection during CosMx data processing. The FOVs were selected by prioritizing specific features such as insulitic islets, islets with few insulin-positive cells, insulin-negative islets, and areas of inflammation in acinar tissue. The gene panel used for spatial imaging included 1010 genes, including 1000 genes from the Human Universal Cell Characterization RNA Panel and 10 additional custom genes selected for this project. The imaging experiments using CosMX were performed at NanoString (Seattle, WA). Cell segmentation was performed by NanoString using Giotto (69), which included using immunofluorescence for glucagon to mark islets, CD3 or CD45 to mark immune cells, and PanCK for ductal cells + 4',6-diamidino-2-phenylindole.

Quality control and transcriptomic clustering of segmented cells

For downstream analysis of spatial transcriptomes, we used the Python toolkits Scanpy (70) and Squidpy (22). For each slide, we imported matrices containing the gene expression, metadata, and positions of segmented cells. We defined a unique cell name and created a merged anndata object with data from all the slides. We adopted a standard filtering strategy, removing cells with less than 10 detected genes and removing genes detected in less than 300 cells. We then normalized the

counts per cell, such that every cell has the same total count after normalization (1×10^6) , and we log-transformed the counts.

Clustering

Gene expression

After individual sample quality control, high-quality barcodes from single modality snRNA-seq and the RNA modality of our multiome data were clustered for 40 samples (32 snRNA and 8 snRNA multiome) using Seurat (v4.3) (71). Quality control metrics such as high mitochondrial percentage (>1%), high number of genes detected (>4000 genes), and high number of RNA counts (>7500) were used to remove low-quality barcodes. A combined clustering was created using principal components (PCs) from gene expression. We used Harmony (20) (v1.0.3) to correct the PCs for batch effects across samples, sex, and sequencing technology. Clusters were removed with low number of cells (<10 cells) and with quality metrics such as the number of detected genes and RNA counts lower than other clusters. Additional doublet cells were removed on the basis of the expression of 2+ canonical markers from unrelated cell types. The final clustering resolution of 0.5 was determined empirically based on maximizing the recovery of known pancreatic cell types and subtypes as distinct clusters.

We leveraged gene expression profiles specific to the wide array of pancreatic cells from previous work to broadly label each snRNA-seq cluster as one of the following types: α (GCG), β (INS), endothelial (PLVAP), lymphatic endothelial (FLT4), ductal (CFTR), acinar (REG1A), stellate (PDGFRB), and variety of immune cells including T cells (CD3D), macrophages (C1QC), and mast cells (KIT) (table S2). Using cell type markers previously used to annotate cell type and subtype populations such as activated stellate (COL6A3) and quiescent stellate (SPARCL1), we were able to annotate these clusters. We identified previously characterized ductal subtype MUC5b ductal cells from the presence of known marker genes such as MUC5B, TIFF3, and CRISP3 (52).

Marker genes of acinar subclusters were identified using DESeq2 (72) (v1.34), followed by gene set enrichment of subcluster marker genes in Kyoto Encyclopedia of Genes and Genomes (KEGG) (73–75) and REACTOME (76) pathways using the fgsea package (v1.20) in R. Briefly, this was done by first creating two sets of sample pseudobulk count matrices of SoupX corrected gene expression for each cell type, one set which has the summation of count per sample per gene for that cell type and another with the summation of counts per sample per gene for all other cell types. We then performed DESeq for each cell type by concatenating these two matrices as our input and using cell type as the outcome variable with sample ID as a covariate.

Accessible chromatin

We first merged 40 samples (32 snATAC samples and 8 multiome snATAC samples) from 29 donors using read counts in 5-kb windows using Signac (77) (v1.9.0). We then performed latent semantic indexing of the combined snATAC data using Signac (77). Harmony (v1.0.3) was used to correct for batch effects using the covariates sample, sex, and sequencing technology (20). Clustering was performed on the batch-corrected PCs using graph-based Leiden clustering. We removed nuclei with a TSSe score < 2 and removed clusters with less than 10 cells or with overall lower-quality metrics, such as fraction of read in peaks, number of ATAC fragments per barcode, and fraction of reads in promoters compared to other clusters. After an initial window-based clustering, we called peaks using MACS2 (78) (v2.2.7.1) (parameters: -q 0.05 --nomodel --keep-dup

all) on each cluster and then repeated the entire clustering process using a consensus set of peaks merged across clusters. Additional doublets were manually removed based off the presence of promoter accessibility of other cell type marker genes. This was done using nine known marker genes (*INS*, *GCG*, *REG1A*, *REG2B*, *CTRB2*, *PRSS1*, *PRSS2*, *CFTR*, and *C1QC*); promoter region was considered 2 kb upstream of the TSS. Data were clustered again after the removal of doublets. The clustering resolution of 0.5 was defined empirically based on maximizing the recovery of known pancreatic cell types and subtypes as distinct clusters. To label cell types, we first assigned gene names to peaks that overlapped 2 kb upstream of TSS and gene body using the gene activity function in Signac and then determined gene activity in established marker genes for each cell type and subtype.

We next performed label transfer on the snATAC object using our gene expression map as reference and the peak-based chromatin data as query in Signac. Because of the size of the chromatin data, before label transfer, we randomly split the barcodes in the object into smaller subsets. We used the 2k most highly variable features from the gene expression map to derive transfer anchors using canonical correlation analysis. These anchors were then used to transfer to the chromatin map using the TransferData function in Seurat (v4.3). After each subset object was done with label transfer, we merged the objects and reclustered all the chromatin data together using the same methods described above. Last, we removed cells with low prediction scores (max.predicted.score < 0.5), and all cells passing this threshold were labeled with the predicted cell type annotation. For acinar cells, we summed the prediction scores of all acinar subtypes then filtered by a combined acinar max.predicted.

To determine the accuracy of label transfer, we used single-cell multiome data where the identity of the accessible chromatin profile is known from the paired gene expression profile. Since the gene expression and chromatin profiles for these nuclei were analyzed separately, we could use them as an independent check. We identified multiome barcodes present in both chromatin and gene expression maps and then calculated the percentage of accessible chromatin barcodes with matching cell type assignments in label transfer and from the paired gene expression profile. Because of the limited transferring of subtypes in the chromatin modality, we calculated a percentage at both the cell type and subtype levels.

Clustering of segmented cells and cell type annotation in spatial data

To cluster the segmented cells, we first integrated the samples using scVI v1.1.2 (79). We performed integration by condition using the slide as a categorical covariate. We then used the latent representation to create a shared nearest-neighbor graph and compute Uniform Manifold Approximation and Projection (UMAP) for twodimensional visualization. We performed hierarchical clustering on the scVI latent space at resolutions of 0.5 and 0.7, and we identified 15 and 16 transcriptomic clusters for ND and T1D, respectively. To annotate cell types, we identified marker genes enriched in each cluster for knowledge-based cell type annotation. We detected endocrine cells by hormone expression, β (INS and IAPP) and α (GCG and TTR); we also identified exocrine cells positively expressing epithelial marker EPCAM, ductal (SOX9 and KRT19), and acinar (EGF, DLL1, and JAG1); we further annotated endothelial cells (PECAM1) and VWF), fibroblasts (VIM and COL1A1), immune cells (CD4 and CD8A), and mast cells (CPA3 and TPSAB1).

Cell type label transfer from reference snRNA-seq data

To achieve a finer annotation on the spatial context, we transferred the cell type labels from the dissociated reference to the spatial data using spatial mapping function from moscot v0.3.5 (21). First, we performed pseudo-bulking of dissociated data using decoupler v1.6.0 (28). We found the optimal combination of parameters for the spatial mapping task by hyperparameter tunning per FOV, and we used cosine distance between the modalities. For the annotation mapping, we selected the label of the annotated cell with the highest matching probability.

Identification of spatial cellular neighborhoods

Cellular neighborhoods in the spatial context were computed per FOV using the squidpy (22) function spatial_neighbors, where we used generic coordinates and considered 30 nearest neighbors.

Identification and annotation of multicellular spatial niches

To identify multicellular niches, we computed the covet representation implemented in envi v0.3.0 (23) per FOV. We used the default parameters, which included 64 genes to represent the covariance matrix. We then created a shared nearest-neighbor graph using the covet representation and performed unsupervised Leiden clustering with a resolution of 0.2. To annotate the clusters, we evaluated the relative cell type abundance in each group per FOV and performed hierarchical clustering. We aggregated "acinar basal," "acinar high-enzyme (enz)," "acinar signal," and "acinar signaling (sig)/differentiation (diff)" subtypes in the acinar niche, "ductal" and "MUC5b ductal" subtypes in the ductal niche, " α ," " β ," and " δ " subtypes in the endocrine niche, and "act stellate," "Q. stellate," "endothelial," "macrophage," and "T cells" in the connective tissue niche.

Downstream analysis

Final peak calling and signal tracks

Cell type–specific set of chromatin peaks were derived using MACS2 (78) v2.2.7.1 on the final cell type annotations of our chromatin map using the following parameters -q 0.05 --nomodel --keep-dup all. These peak calls were used to accessible chromatin signal tracks in UCSC genome browser (80).

Marker CREs

Cell type–specific cREs were derived for each cell type and subtype. We first created a set of union peaks across the whole dataset. This was achieved by limiting peak size for all called peaks to 300 bp by centering any peaks larger than 300 bp at their summit and extending coordinates 150 bp in either direction. We grouped peaks based on overlap to create clusters of peaks. Within each cluster, the peak with the highest read count at its summit was identified as the reference peak for the region. We then generated a list of peaks that did not overlap any of the reference peaks and iteratively identified additional reference peaks again until no peaks remained.

We used this set of union peaks to calculate two sets of sample level pseudo-bulk matrices per cell type as follows: First, we aggregated the number of ATAC fragments within peaks per donor per cell type and then, for each cell type, created a second matrix with the summation of fragments from all other cell types. Normalized count matrices were generated by dividing the number of fragments within a peak by the total number of fragments for that sample in that cell type and then multiplying by a scaling factor (1×10^6). Cell type–specific regulatory elements were then determined for each cell type by comparing the normalized count matrix for a given cell type with the normalized count matrix of all other cell types summed

together. To test enrichment of a given peak for each cell type, we performed a logistic regression model using sample ID as a covariate and corrected for multiple tests using the Benjamini-Hochberg correction method (FDR < 0.1). We limited the marker cREs per cell type to the top 5000 cREs ranked by fold change. We performed motif enrichment of marker cREs for each cell type compared to a background of all cREs in the cell type using HOMER (81) v5.0.1 and retained enriched motifs at FDR < 0.01. We also tested for gene set enrichment in marker cREs using GREAT (82) (v4.0.4).

Normalized gene expression levels

We derived normalized gene expression profiles for each cell type by creating aggregate count matrices by donor per cell type. Counts were normalized per million (CPM) by dividing the counts for each gene by the total counts per donor and multiplying by 1×10^6 .

Cell type proportion changes

We first scaled the counts for each cell type in a sample to 10,000 cells per sample. For several cell types, we excluded samples with abnormally high counts (6278 for β and δ ; 6393 for T cells and B cells; 6375 for MUC5b $^+$ ductal cells). We then created a linear model of the log-transformed counts as a function of disease status (ND, ND AAB $^+$, recent-onset T1D, and long-standing T1D), age, sex, and body mass index (BMI), as well as a linear model without disease status. We performed comparison of the models using a likelihood ratio test in package lmtest in R and considered P values from the test significant at 0.05.

Differential gene expression

To determine disease-related changes in gene expression, we performed differential analysis using DESeq2 (72) v1.34. Using snRNAseq data, we derived pseudo-bulk count matrices for each cell type by aggregating all barcodes of a donor for each gene on a per cell type basis. We created the count matrices from the SoupX (68)-corrected expression counts and then rounded counts in the matrix to the nearest integer. We included sex, age, and BMI, as well as proportion of β cells, as covariates in the model. For endocrine cell types, we included expression counts from scRNA-seq of 48 donors from the HPAP consortium (31) derived from a previously created single-cell map (15) and included an additional covariate in the model for cohort. For a given cell type, we only used samples with at least 20 cells, except for long-standing T1D β cells where we included all samples, and donor 6234 was excluded from analyses due to aberrant numbers of endocrine cells. For nonendocrine cell types, genes were tested if detected in at least two samples per condition and had >10 counts across all tested conditions, while for endocrine cell types, genes were tested if present in at least half of the donors per condition. We further excluded genes for each cell type that are established marker genes for a different cell type. Multiple test correction was performed using the Benjamini-Hochberg correction, and we considered genes significant at FDR < 0.1.

Differential cRE accessibility

Using cell type–specific peak calls from MACS2 (78) v2.2.7.1 per cell type, we created peak by barcode fragment count matrices all snATAC-seq donors for each disease condition. Peaks with low accessibility were removed from analysis, as determined by the average accessibility of peak across all samples less than median accessibility of all peaks across all samples. In addition, for each cell type, samples were removed with <10 barcodes in that cell type. Last, cell types with less than 10 cells were not used in this analysis. We tested each disease condition against ND using glmer (83) in R using the logistic regression model [peak accessibility ~ disease + scale (FRiP) +

scale (count) + (1|sample)] using a binary peak count matrix. We used the fixed covariates of fraction reads in peak (FRiP) and ATAC fragment count (count) to account for sequencing depth variation and used sample ID as a random effect to adjust for sample variation. We considered sample as a random effect to mediate pseudoreplication of barcodes from the same donors. Cell types with more than 30,000 cells were subsampled down to 10,000 for this analysis. Fold change was calculated by dividing the average accessibility of peaks between conditions. Multiple test correction was performed using the Benjamini-Hochberg method, and we considered cREs significant at FDR < 0.1.

Pathway enrichment during T1D using gene expression input

To test for pathways enriched by disease, we performed gene set enrichment analysis (GSEA) (84, 85). Using the results from our differential expression analysis, input genes were ranked using the following formula $[-\log_{10}(P \text{ value}) \times \log_2 \text{ fold change}]$, and the fgsea package (v1.20) in R was run using both KEGG (73–75) and REACTOME (86–92) databases [parameters: eps = 0.0, min-Size = 0, maxSize = 1000]. Pathways were considered significant using FDR < 0.1.

Motif enrichment

We used chromVAR (26) to measure z-scored motif accessibility in snATAC-seq data. To do so, we prepared peak count data for input to chromVAR by converting the fixed peak sparse count matrix into a SummarizedExperiment and estimated Guanine/Cytosine (GC) content bias using chromVAR built in method (26). Human TF motifs from JASPAR 2022 (93) were accessed using the JASPAR2022 Bioconductor package in R, and motifs were annotated to peaks using motifmatchr (v.1.21.0) in R. The SummarizedExperiment and motif annotations were used as inputs into chromVAR computeDeviations function to derive GC bias-corrected motif accessibility z-scores.

Motifs enriched in cell types

TF motifs were filtered for those with an accessibility of >1.2 based on chromVAR built-in computeVariability function. Cell types with <50 cells were excluded. Cell type motif accessibility *z*-scores were averaged and plotted with pheatmap (v1.0.13) and RColorBrewer (v1.1-3) in R.

Motifs enriched in acinar subtypes

After subsetting the motif matrix to barcodes from acinar cells, we averaged motif accessibility of each acinar subtype per sample and then tested each motif using a two-way analysis of variance (ANOVA) across acinar subtypes also including a donor variable. We then calculated FDR from the *P* values using the *q* value package in R. To identify which specific subtype a significant motif was most enriched in, motifs were further tested using a two-way ANOVA comparing motif accessibility within the subtype to the average motif accessibility for the other acinar subtypes together also including a donor variable. *P* values for each motif were corrected by the Holm's method. Motifs were annotated to subclusters based on being significant in the pan-subtype ANOVA, significant in the post hoc ANOVA with Holm's correction, and having the highest average deviation score in the given cluster.

Motif differential accessibility

To identify motifs with differential accessibility across disease states, we used a linear mixed model using the lmerTest (v3.1-3) package in R. We identified motifs in a cell type enriched in cREs with altered activity in ND AAB⁺ or T1D. For these motifs, accessibility was modeled by barcode using encoded variables to contrast autoantibody, recent-onset and long-duration T1D against ND controls. Scaled fractions of reads in peaks and scaled number of

counts were used as fixed effect covariates, and a random effect for sample was used to account for pseudo-replication. Samples with <10 cells in the cell type were excluded, and cell types with <50 cells or disease states with <20 cells and three samples were not tested. We obtained P values from the resulting models. Motif accessibility was averaged by sample and disease state to make box plots. Motif accessibility per condition was generated by averaging sample average motif accessibility, and volcano plots were generated by comparing difference in motif accessibility versus $-\log_{10} q$ values, with a difference threshold of 0.25 and q value of 0.05 for dashed lines and coloring and labeling of samples.

Motif enrichment in differential accessible CREs

To identify TF motifs enriched in cRE differential accessibility in each cell type, we used HOMER (81) (v5.0.1). For each cell type, we identified cREs with nominal association (uncorrected P < 0.05) and split cREs by fold change as input and user HOMER function findMotifs-Genome with a background of all cREs for the cell type with a size parameter of 200 and a masked version of the human genome hg38. Multiple test correction was done using the Benjamini-Hochberg method, and significant motifs were considered at FDR < 0.1.

ABC analysis

To link cREs to target genes, we used ABC (94) v0.2. This was done by first creating .bam files for each cell containing only barcodes from the accessible chromatin map. Since the HiC reference panel used was in hg19 genome build, cell type bams and peaks were converted to hg19 using CrossMap (95) v0.6.3, and we called peaks for each cell type with MACS2 v2.2.7.1 using this genome build. To further improve enhancer activity prediction, we used publicly available Histone H3 lysine 27 acetylation (H3K27ac) chromatin immunoprecipitation sequencing data for acinar, ductal, α , β , and δ cells (96). We predicted candidate regions and enhancer activity for each cell type using the following flags: --peakExtendFromSummit 250, --nStrongestPeaks 150000 and a list of genes with nonzero expression (CPM > 0) in that cell type. After ABC analysis, links were converted back to hg38 using CrossMap. We identified genes with cell type-specific cRE link profiles by calculating the proportion of the total number of ABC links for that gene by cell type and calculating Shannon entropy based on the proportion.

Constructing TF GRNs

To determine GRNs, we constructed units of TFs linked to cCREs linked to genes. We first used a position frequency matrix (PFMatrixList object) of TF DNA binding preferences from the JASPAR 2022 database (93) and width-fixed peaks (97) as input to perform TF motif analysis. We used the "matchMotifs" function in the R package motifmatchr (v.1.21.0) to infer cell type–specific cREs bound by each TF. We linked cREs bound by each TF to target genes based on proximity to the gene promoter (±5 kb) of a TSS in GENCODE V19 or through ABC links (94, 98) at a score cutoff of 0.015. TF GRNs were retained for analysis if the network included fewer genes and then the 90th percentile of number of genes linked to a given TF. In addition to ensure that TF GRNs were active in the associated cell type, we filtered TF GRNs based on cell type CPM > 1 for the TF gene.

Identification of cell type-specific TF modules and pathway enrichment

For each pancreatic cell population, we identified pathways and TF modules enriched using our identified marker CREs. Briefly, this was done for each cell type by deriving CREs associated with KEGG

and REACTOME paths using the bedtools intersection TF module gene–linked CREs with union peaks accessible in that cell type. These union peak–based pathways were tested for enrichment using the fgsea package (v1.20) in R. We used the logistic regression marker CRE results to rank peaks using the following formula [$-\log_{10}\left(P\right)$ value) $\times\log_{2}$ fold changes]. Similarly, we tested for TF modules enriched in each cell type by defining union peaks associated with a TF either proximally or through ABC and then using the logistic regression marker CRE results to rank peaks and test for enrichment using fgsea. For both analyses, we used Benjamini-Hochberg for multiple test correction and retained results with an FDR < 0.1.

Identification of TF GRNs linked to biological pathways altered in T1D

To identify regulators of enriched pathways for each cell type, we next tested enrichment of each TF module in pathways identified in our fgsea analysis. We performed the Fisher's exact test to test for overlap in genes in each TF GRN and genes in each biological pathway in KEGG and REACTOME for each cell type. We performed multiple test correction using FDR and considered TF GRNs linked to a pathway at FDR < 0.1. Next, we filtered results to biological pathways with significantly altered expression in T1D and TF motifs belonging to TF subfamilies with differentially accessibility in T1D from chromVAR (26) results.

Genetic association enrichment

We tested for enrichment of T1D-associated variants using summary statistics from a published genome-wide association study (5). We defined groups of cREs in multiple ways; first, by identifying all cREs in each cell type linked to genes in each biological pathway in KEGG and REACTOME using ABC and promoter proximity links and, second, by identifying cREs in each cell type in GRNs for each TF. We calculated Bayes factors for each variant with minor allele frequency > 0.05 genome-wide, excluding all variants at the MHC locus, using the method of Wakefield (99). We then tested for enrichment of T1D-associated variants in groups of cREs genome-wide using fgwas v0.3.6 (37) with a block size (-k) of 2500.

We overlapped cREs in each cell type with credible sets of variants at known T1D signals from a published fine-mapping study. We further determined which cREs had at least nominal evidence (uncorrected P < 0.05) for differential accessibility in ND AAB⁺ or T1D.

Cell-cell interactions

The gene expression data were prefiltered before running CellChat (39) v1.1.3. First, any cell type represented by <20 cells for a sample was excluded. Next, cell types that appeared in fewer than two samples within a control or disease group were excluded from that group.

We considered a ligand expressed in a specific cell type if the average expression of the ligand in the cell type was greater than half the SD of its average expression across all cells in at least two samples. After applying these filters, we ran CellChat using the RNA data slot of the Seurat object across the entire CellChat database (CCdb) with default parameters except for "trim = 0" in the "computeCommunProb" command and "thresh = 1" in the "subsetCommunication" command (39). Each control and disease group was processed independently. Ligands from the CCdb were grouped into categories by manual curation using UniProt (100) and GeneCard (101, 102) (listed in table S14). Gene families were downloaded using biomart in the Bioconductor package (v3.1) in R.

Results from different conditions were consolidated and subjected to FDR correction using the Benjamini-Hochberg method with the *q* value package in Bioconductor (v3.21) in R. Predicted interactions

with an FDR < 0.1 and an interaction strength (IS) above the second quartile were considered for downstream interpretation. To remove residual background contamination due to highly expressed genes, the following interactions were blacklisted in all cell sources except the ones listed: INS in β cells, GCG in α cells, SST in δ cells, PRSS1/2/3 in acinar cells, CD8A, CD8B, and CD8B2 in T cells, and CD4 in T cells and macrophages.

To assess the significance of differences between conditions, we randomly permuted sample IDs among conditions and reperformed CellChat analysis $100\times$ and compared outcomes with the observed results. The permutations were filtered using the same parameters as for the observed data. Next, we aggregated the IS across different "units" by summing all LR pairs within a unit and normalizing this sum by the number of significant interactions for each condition. We then quantified the difference in effect size (IS – effect size) across contrasts: ND AAB⁺ versus ND, recent-onset T1D versus ND, and long-duration T1D versus ND. A P value was calculated by comparing the observed results against the simulations using the formula: the number of instances where simulation IS – effect size exceeded observational IS – effect size divided by the number of permutations. P values were corrected for multiple tests using Benjamini-Hochberg. We considered interactions with FDR < 0.1 significant.

Functional analysis of spatial genomic profiles

We inferred TF and pathway activities using Liana v1.1.0 (32). For TF activity inference, we use the cell type–specific GRNs derived from single-cell multiome. We then fit a univariate linear model to infer the interaction weights. To identify cell type–specific TFs, we performed a t test overestimating the variance of each group and filtered TFs according to an adjusted P < 0.05. We inferred pathway activities using the PROGENy model (32). We used weights of the top 500 responsive genes ranked by P value. We then fit a multivariate linear model to obtain the weights corresponding to pathway interactions. As with the TF activity analyses, we identified cell type–specific pathways by performing a t test overestimating the variance of each group.

Cell-cell communication

We analyzed cell-cell communication in spatial transcriptomic data using SpatialDM v0.2.0 (40). We performed the analysis per condition, and per donor, having each FOV as technical replicate. For this study, the parameters l and cutoff were set to 100 and 0.2 to represent the spatial context. In addition, we computed the weight matrix using the single-cell mode, and we extracted the LR interactions from the CCdb (39). To compute the global Moran's I score and the local spot detection, we used the z-score method.

EndoC-Bh1 stimulation experiments and RNA-seq

A total of 25,000 EndoC-BH1 cells were seeded in media composed of Dulbecco's modified Eagle's medium (Corning, 10014CV), 2% BSA (Sigma-Aldrich, A1470), 3.5×10^{-4} 2-mercaptoethanol (Gibco, 21985023), 0.12% nicotinamide (MilliporeSigma, 481907), transferrin (5.5 ng/ml; MilliporeSigma, T8158), sodium selenite (6.7 pg/ml; Sigma-Aldrich, 214485), and 1% penicillin-streptomycin (Gibco, 15140122) on a 96-well (CellTreat Scientific Products, 229105) plate coated with ECM (Sigma-Aldrich, E1270) and fibronectin (Sigma-Aldrich, F1141). The recombinant protein concentrations used were as follows: PGRN (1 µg/ml) and BMP5 (50 ng/ml). EndoC- β H1 cells were obtained from Human Cell Design. RNA was isolated using the RNeasy Mini Kit (QIAGEN) from EndoC-Bh1 cells either stimulated or unstimulated with each ligand. Samples included three replicates each for PGRN and its untreated controls and six

replicates each for BMP5 and its untreated controls. RNA integrity was assessed using a 2200 TapeStation (Agilent Technologies), and all samples achieved an RNA integrity number greater than 7. Ribodepleted total RNA libraries were prepared using the TruSeq Stranded Total RNA Library Prep Gold kit (Illumina, catalog no. 20020599) and sequenced at the UCSD Institute for Genomic Medicine on an Illumina NovaSeq S4 platform.

Bulk RNA-seq analysis

Quality control of the sequencing data was assessed using FastQC (v0.12.0). Transcript quantification was performed using Salmon (103) with default parameters and the hg38 reference indexes. Counts were imported into R using the tximport (104) package, and genes with fewer than 10 reads were excluded. Differential gene expression analysis was conducted using DESeq2 (72), applying an FDR threshold of <0.1. For pathway enrichment analysis, the fgsea package (v1.20) in R was used using the "stat" column from DESeq2 results. The fgsea analysis was restricted to gene sets containing >10 and <500 terms. Pathways were corrected for multiple testing using FDR < 0.1, and only pathways in KEGG (73–75) or REACTOME (86, 87, 89, 90) were considered.

Supplementary Materials

The PDF file includes:

Figs. S1 to S15 Legends for tables S1 to S17

Other Supplementary Material for this manuscript includes the following: Tables S1 to S17

REFERENCES AND NOTES

- A. Lehuen, J. Diana, P. Zaccone, A. Cooke, Immune cell crosstalk in type 1 diabetes. Nat. Rev. Immunol. 10, 501–513 (2010).
- K. Eguchi, R. Nagai, Islet inflammation in type 2 diabetes and physiology. J. Clin. Invest. 127, 14–23 (2017).
- 3. J. Boldison, F. S. Wong, Immune and pancreatic β cell interactions in type 1 diabetes. *Trends Endocrinol. Metab.* **27**, 856–867 (2016).
- M. Fasolino, G. W. Schwartz, A. R. Patil, A. Mongia, M. L. Golson, Y. J. Wang, A. Morgan, C. Liu, J. Schug, J. Liu, M. Wu, D. Traum, A. Kondo, C. L. May, N. Goldman, W. Wang, M. Feldman, J. H. Moore, A. S. Japp, M. R. Betts, HPAP Consortium, A. Naji, K. H. Kaestner, G. Vahedi, Single-cell multi-omics analysis of human pancreatic islets reveals novel cellular states in type 1 diabetes. *Nat. Metab.* 4, 284–299 (2022).
- J. Chiou, R. J. Geusz, M.-L. Okino, J. Y. Han, M. Miller, R. Melton, E. Beebe, P. Benaglio, S. Huang, K. Korgaonkar, S. Heller, A. Kleger, S. Preissl, D. U. Gorkin, M. Sander, K. J. Gaulton, Interpreting type 1 diabetes risk with genetics and single-cell epigenomics. *Nature* 594, 398–402 (2021).
- R. Mallone, C. Halliez, J. Rui, K. C. Herold, The β-cell in type 1 diabetes pathogenesis: A victim of circumstances or an instigator of tragic events? *Diabetes* 71, 1603–1610 (2022).
- M. A. Atkinson, The pathogenesis and natural history of type 1 diabetes. Cold Spring Harb. Perspect. Med. 2, a007641 (2012).
- C. Pihoker, L. K. Gilliam, C. S. Hampe, Å. Lernmark, Autoantibodies in diabetes. *Diabetes* 54 (Suppl. 2), S52–S61 (2005).
- P. J. Bingley, M. R. Christie, E. Bonifacio, R. Bonfanti, M. Shattock, M.-T. Fonte, G.-F. Bottazzo, E. A. M. Gale, Combined analysis of autoantibodies improves prediction of IDDM in islet cell antibody-positive relatives. *Diabetes* 43, 1304–1310 (1994).
- P. J. Bingley, E. Bonifacio, A. J. K. Williams, S. Genovese, G. F. Bottazzo, E. A. M. Gale, Prediction of IDDM in the general population: Strategies based on combinations of autoantibody markers. *Diabetes* 46, 1701–1710 (1997).
- G. Fousteri, E. Ippolito, R. Ahmed, A. Rahim Hamad, Beta-cell specific autoantibodies: Are they just an indicator of type 1 diabetes? Curr. Diabetes Rev. 13, 322–329 (2017).
- R. A. Oram, E. K. Sims, C. Evans-Molina, Beta cells in type 1 diabetes: Mass and function; Sleeping or dead? *Diabetologia* 62, 567–577 (2019).
- M. Mănescu, I. Mănescu, A. Grama, A review of stage 0 biomarkers in type 1 diabetes: The holy grail of early detection and prevention? J. Pers. Med. 14, 878 (2024).
- S. Preissl, K. J. Gaulton, B. Ren, Characterizing cis-regulatory elements using single-cell epigenomics. *Nat. Rev. Genet.* 24, 21–43 (2023).

- R. M. Elgamal, P. Kudtarkar, R. L. Melton, H. M. Mummey, P. Benaglio, M.-L. Okino, K. J. Gaulton, An integrated map of cell type–specific gene expression in pancreatic islets. *Diabetes* 72, 1719–1728 (2023).
- D. Bressan, G. Battistoni, G. J. Hannon, The dawn of spatial omics. Science 381, eabq4964 (2023).
- A. Pugliese, Insulitis in the pathogenesis of type 1 diabetes. *Pediatr. Diabetes* 17, 31–36 (2016).
- P. Benaglio, H. Zhu, M.-L. Okino, J. Yan, R. Elgamal, N. Nariai, E. Beebe, K. Korgaonkar, Y. Qiu, M. K. R. Donovan, J. Chiou, G. Wang, J. Newsome, J. Kaur, M. Miller, S. Preissl, S. Corban, A. Aylward, J. Taipale, B. Ren, K. A. Frazer, M. Sander, K. J. Gaulton, Type 1 diabetes risk genes mediate pancreatic beta cell survival in response to proinflammatory cytokines. *Cell Genom.* 2, 100214 (2022).
- The Type 1 Diabetes TrialNet Study Group, P. J. Bingley, D. C. Boulware, J. P. Krischer, The implications of autoantibodies to a single islet antigen in relatives with normal glucose tolerance: Development of other autoantibodies and progression to type 1 diabetes. *Diabetologia* 59, 542–549 (2016).
- I. Korsunsky, N. Millard, J. Fan, K. Slowikowski, F. Zhang, K. Wei, Y. Baglaenko, M. Brenner, P.-R. Loh, S. Raychaudhuri, Fast, sensitive and accurate integration of single-cell data with Harmony. *Nat. Methods* 16, 1289–1296 (2019).
- D. Klein, G. Palla, M. Lange, M. Klein, Z. Piran, M. Gander, L. Meng-Papaxanthos, M. Sterr, L. Saber, C. Jing, A. Bastidas-Ponce, P. Cota, M. Tarquis-Medina, S. Parikh, I. Gold, H. Lickert, M. Bakhti, M. Nitzan, M. Cuturi, F. J. Theis, Mapping cells through time and space with moscot. *Nature* 638, 1065–1075 (2025).
- G. Palla, H. Spitzer, M. Klein, D. Fischer, A. C. Schaar, L. B. Kuemmerle, S. Rybakov, I. L. Ibarra, O. Holmberg, I. Virshup, M. Lotfollahi, S. Richter, F. J. Theis, Squidpy: A scalable framework for spatial omics analysis. *Nat. Methods* 19, 171–178 (2022).
- D. Haviv, J. Remšík, M. Gatie, C. Snopkowski, M. Takizawa, N. Pereira, J. Bashkin,
 Jovanovich, T. Nawy, R. Chaligne, A. Boire, A.-K. Hadjantonakis, D. Pe'er, The covariance environment defines cellular niches for spatial inference. *Nat. Biotechnol.* 43, 269–280 (2025).
- M. Ali, M. Kuijs, S. Hediyeh-zadeh, T. Treis, K. Hrovatin, G. Palla, A. C. Schaar, F. J. Theis, GraphCompass: Spatial metrics for differential analyses of cell organization across conditions. *Bioinformatics* 40, i548–i557 (2024).
- T. Stuart, A. Butler, P. Hoffman, C. Hafemeister, E. Papalexi, W. M. Mauck, Y. Hao, M. Stoeckius, P. Smibert, R. Satija, Comprehensive integration of single-cell data. *Cell* 177, 1888–1902.e21 (2019).
- A. N. Schep, B. Wu, J. D. Buenrostro, W. J. Greenleaf, chromVAR: Inferring transcriptionfactor-associated accessibility from single-cell epigenomic data. *Nat. Methods* 14, 975–978 (2017).
- K. Zhang, J. D. Hocker, M. Miller, X. Hou, J. Chiou, O. B. Poirion, Y. Qiu, Y. E. Li, K. J. Gaulton, A. Wang, S. Preissl, B. Ren, A single-cell atlas of chromatin accessibility in the human genome. *Cell* 184, 5985–6001.e19 (2021).
- P. Badia-i-Mompel, J. Vélez Santiago, J. Braunger, C. Geiss, D. Dimitrov, S. Müller-Dott, P. Taus, A. Dugourd, C. H. Holland, R. O. Ramirez Flores, J. Saez-Rodriguez, decoupleR: Ensemble of computational methods to infer biological activities from omics data. *Bioinform. Adv.* 2, vbac016 (2022).
- R. K. Mitchell, M.-S. Nguyen-Tu, P. Chabosseau, R. M. Callingham, T. J. Pullen, R. Cheung, I. Leclerc, D. J. Hodson, G. A. Rutter, The transcription factor *Pax6* is required for pancreatic β cell identity, glucose-regulated ATP synthesis, and Ca²⁺ dynamics in adult mice. *J. Biol. Chem.* 292, 8892–8906 (2017).
- M. Jiang, A. C. Azevedo-Pouly, T. G. Deering, C. Q. Hoang, D. DiRenzo, D. A. Hess,
 F. Konieczny, G. H. Swift, R. J. MacDonald, MIST1 and PTF1 collaborate in feed-forward regulatory loops that maintain the pancreatic acinar phenotype in adult mice. *Mol. Cell. Biol.* 36, 2945–2955 (2016).
- K. H. Kaestner, A. C. Powers, A. Naji, HPAP Consortium, M. A. Atkinson, NIH initiative to improve understanding of the pancreas, islet, and autoimmunity in type 1 diabetes: The Human Pancreas Analysis Program (HPAP). *Diabetes* 68, 1394–1402 (2019).
- D. Dimitrov, P. S. L. Schäfer, E. Farr, P. Rodriguez-Mier, S. Lobentanzer, P. Badia-i-Mompel, A. Dugourd, J. Tanevski, R. O. Ramirez Flores, J. Saez-Rodriguez, LIANA+ provides an all-in-one framework for cell-cell communication inference. *Nat. Cell Biol.* 26, 1613–1622 (2024).
- T. P. Foster, B. Bruggeman, M. Campbell-Thompson, M. A. Atkinson, M. J. Haller,
 D. A. Schatz, Exocrine pancreas dysfunction in type 1 diabetes. *Endocr. Pract.* 26, 1505–1513 (2020).
- J. Matsui, T. Wakabayashi, M. Asada, K. Yoshimatsu, M. Okada, Stem cell factor/c-kit signaling promotes the survival, migration, and capillary tube formation of human umbilical vein endothelial cells. J. Biol. Chem. 279, 18600–18607 (2004).
- C.-H. Wang, S. Verma, I.-C. Hsieh, A. Hung, T.-T. Cheng, S.-Y. Wang, Y.-C. Liu, W. L. Stanford, R. D. Weisel, R.-K. Li, W.-J. Cherng, Stem cell factor attenuates vascular smooth muscle apoptosis and increases intimal hyperplasia after vascular injury. *Arterioscler. Thromb. Vasc. Biol.* 27, 540–547 (2007).
- G. Wang, J. Chiou, C. Zeng, M. Miller, I. Matta, J. Y. Han, N. Kadakia, M.-L. Okino, E. Beebe, M. Mallick, J. Camunas-Soler, T. Dos Santos, X.-Q. Dai, C. Ellis, Y. Hang, S. K. Kim,

- P. E. MacDonald, F. R. Kandeel, S. Preissl, K. J. Gaulton, M. Sander, Integrating genetics with single-cell multiomic measurements across disease states identifies mechanisms of beta cell dysfunction in type 2 diabetes. *Nat. Genet.* **55**, 984–994 (2023).
- J. K. Pickrell, Joint analysis of functional genomic data and genome-wide association studies of 18 human traits. Am. J. Hum. Genet. 94, 559–573 (2014).
- M. Ramos-Rodríguez, H. Raurell-Vila, M. L. Colli, M. I. Alvelos, M. Subirana-Granés,
 J. Juan-Mateu, R. Norris, J.-V. Turatsinze, E. S. Nakayasu, B.-J. M. Webb-Robertson,
 J. R. J. Inshaw, P. Marchetti, L. Piemonti, M. Esteller, J. A. Todd, T. O. Metz, D. L. Eizirik,
 L. Pasquali, The impact of proinflammatory cytokines on the β-cell regulatory landscape provides insights into the genetics of type 1 diabetes. Nat. Genet. 51, 1588–1595 (2019).
- S. Jin, C. F. Guerrero-Juarez, L. Zhang, I. Chang, R. Ramos, C.-H. Kuan, P. Myung, M. V. Plikus, Q. Nie, Inference and analysis of cell-cell communication using CellChat. *Nat. Commun.* 12, 1088 (2021).
- Z. Li, T. Wang, P. Liu, Y. Huang, SpatialDM for rapid identification of spatially co-expressed ligand-receptor and revealing cell-cell communication patterns. *Nat. Commun.* 14, 3995 (2023).
- J. Dooley, L. Tian, S. Schonefeldt, V. Delghingaro-Augusto, J. E. Garcia-Perez, E. Pasciuto, D. Di Marino, E. J. Carr, N. Oskolkov, V. Lyssenko, D. Franckaert, V. Lagou, L. Overbergh, J. Vandenbussche, J. Allemeersch, G. Chabot-Roy, J. E. Dahlstrom, D. R. Laybutt, N. Petrovsky, L. Socha, K. Gevaert, A. M. Jetten, D. Lambrechts, M. A. Linterman, C. C. Goodnow, C. J. Nolan, S. Lesage, S. M. Schlenner, A. Liston, Genetic predisposition for beta cell fragility underlies type 1 and type 2 diabetes. *Nat. Genet.* 48, 519–527 (2016).
- 42. A. Liston, J. A. Todd, V. Lagou, Beta-cell fragility as a common underlying risk factor in type 1 and type 2 diabetes. *Trends Mol. Med.* 23, 181–194 (2017).
- L. Marroquí, I. Santin, R. S. Dos Santos, L. Marselli, P. Marchetti, D. L. Eizirik, BACH2, a candidate risk gene for type 1 diabetes, regulates apoptosis in pancreatic β-cells via JNK1 modulation and crosstalk with the candidate gene PTPN2. Diabetes 63, 2516–2527 (2014).
- I. Santin, F. Moore, M. L. Colli, E. N. Gurzov, L. Marselli, P. Marchetti, D. L. Eizirik, PTPN2, a candidate gene for type 1 diabetes, modulates pancreatic β-cell apoptosis via regulation of the BH3-only protein Bim. Diabetes 60, 3279–3288 (2011).
- 45. I. Santin, D. L. Eizirik, Candidate genes for type 1 diabetes modulate pancreatic islet inflammation and β -cell apoptosis. *Diabetes Obes. Metab.* **15**, 71–81 (2013).
- J. Størling, F. Pociot, Type 1 diabetes candidate genes linked to pancreatic islet cell inflammation and beta-cell apoptosis. Genes 8, 72 (2017).
- M. L. Colli, F. Moore, E. N. Gurzov, F. Ortis, D. L. Eizirik, MDA5 and PTPN2, two candidate genes for type 1 diabetes, modify pancreatic β-cell responses to the viral by-product double-stranded RNA. *Hum. Mol. Genet.* 19, 135–146 (2010).
- M.-F. Tsan, B. Gao, Heat shock proteins and immune system. J. Leukoc. Biol. 85, 905–910 (2009).
- K. C. Kregel, Invited Review: Heat shock proteins: Modifying factors in physiological stress responses and acquired thermotolerance. J. Appl. Physiol. 92, 2177–2186 (2002).
- M. Bogdani, E. Korpos, C. J. Simeonovic, C. R. Parish, L. Sorokin, T. N. Wight, Extracellular matrix components in the pathogenesis of type 1 diabetes. Curr. Diab. Rep. 14, 552 (2014).
- N. M. Doliba, A. V. Rozo, J. Roman, W. Qin, D. Traum, L. Gao, J. Liu, E. Manduchi, C. Liu, M. L. Golson, G. Vahedi, A. Naji, F. M. Matschinsky, M. A. Atkinson, A. C. Powers, M. Brissova, K. H. Kaestner, D. A. Stoffers, α cell dysfunction in islets from nondiabetic, glutamic acid decarboxylase autoantibody–positive individuals. *J. Clin. Invest.* 132, e156243 (2022).
- L. Tosti, Y. Hang, O. Debnath, S. Tiesmeyer, T. Trefzer, K. Steiger, F. W. Ten, S. Lukassen,
 Ballke, A. A. Kühl, S. Spieckermann, R. Bottino, N. Ishaque, W. Weichert, S. K. Kim, R. Eils,
 C. Conrad, Single-nucleus and in situ RNA-sequencing reveal cell topographies in the human pancreas. *Gastroenterology* 160, 1330–1344.e11 (2021).
- J. Chiou, C. Zeng, Z. Cheng, J. Y. Han, M. Schlichting, M. Miller, R. Mendez, S. Huang, J. Wang, Y. Sui, A. Deogaygay, M.-L. Okino, Y. Qiu, Y. Sun, P. Kudtarkar, R. Fang, S. Preissl, M. Sander, D. U. Gorkin, K. J. Gaulton, Single-cell chromatin accessibility identifies pancreatic islet cell type– and state-specific regulatory programs of diabetes risk. *Nat. Genet.* 53, 455–466 (2021).
- 54. H. E. Thomas, J. A. Trapani, T. W. H. Kay, The role of perforin and granzymes in diabetes. *Cell Death Differ.* **17**, 577–585 (2010).
- A. L. Notkins, Immunologic and genetic factors in type 1 diabetes. J. Biol. Chem. 277, 43545–43548 (2002).
- J. Goulley, U. Dahl, N. Baeza, Y. Mishina, H. Edlund, BMP4-BMPR1A signaling in β cells is required for and augments glucose-stimulated insulin secretion. Cell Metab. 5, 207–219 (2007).
- J. Chmielowiec, W. J. Szlachcic, D. Yang, M. A. Scavuzzo, K. Wamble, A. Sarrion-Perdigones, O. M. Sabek, K. J. T. Venken, M. Borowiak, Human pancreatic microenvironment promotes β-cell differentiation via non-canonical WNT5A/JNK and BMP signaling. *Nat. Commun.* 13, 1952 (2022).
- A. I. Urizar, M. Prause, L. R. Ingerslev, M. Wortham, Y. Sui, M. Sander, K. Williams, R. Barrès, M. R. Larsen, G. L. Christensen, N. Billestrup, Beta cell dysfunction induced by bone morphogenetic protein (BMP)-2 is associated with histone modifications and decreased NeuroD1 chromatin binding. Cell Death Dis. 14, 399 (2023).

- A. Barbu, M. H. Lejonklou, B. Skogseid, Progranulin stimulates proliferation of mouse pancreatic islet cells and is overexpressed in the endocrine pancreatic tissue of an MEN1 mouse model. *Pancreas* 45, 533–540 (2016).
- P. F. Cheung, J. Yang, R. Fang, A. Borgers, K. Krengel, A. Stoffel, K. Althoff, C. W. Yip,
 E. H. L. Siu, L. W. C. Ng, K. S. Lang, L. B. Cham, D. R. Engel, C. Soun, I. Cima, B. Scheffler,
 J. K. Striefler, M. Sinn, M. Bahra, U. Pelzer, H. Oettle, P. Markus, E. M. M. Smeets,
 E. H. J. G. Aarntzen, K. Savvatakis, S.-T. Liffers, S. S. Lueong, C. Neander, A. Bazarna,
 X. Zhang, A. Paschen, H. C. Crawford, A. W. H. Chan, S. T. Cheung, J. T. Siveke, Progranulin mediates immune evasion of pancreatic ductal adenocarcinoma through regulation of MHCI expression. *Nat. Commun.* 13, 156 (2022).
- R. A. Insel, J. L. Dunne, M. A. Atkinson, J. L. Chiang, D. Dabelea, P. A. Gottlieb,
 C. J. Greenbaum, K. C. Herold, J. P. Krischer, Å. Lernmark, R. E. Ratner, M. J. Rewers,
 D. A. Schatz, J. S. Skyler, J. M. Sosenko, A.-G. Ziegler, Staging presymptomatic type 1 diabetes: A scientific statement of JDRF, the Endocrine Society, and the American Diabetes Association. *Diabetes Care* 38, 1964–1974 (2015).
- 62. M. Battaglia, S. Ahmed, M. S. Anderson, M. A. Atkinson, D. Becker, P. J. Bingley, E. Bosi, T. M. Brusko, L. A. DiMeglio, C. Evans-Molina, S. E. Gitelman, C. J. Greenbaum, P. A. Gottlieb, K. C. Herold, M. J. Hessner, M. Knip, L. Jacobsen, J. P. Krischer, S. A. Long, M. Lundgren, E. F. McKinney, N. G. Morgan, R. A. Oram, T. Pastinen, M. C. Peters, A. Petrelli, X. Qian, M. J. Redondo, B. O. Roep, D. Schatz, D. Skibinski, M. Peakman, Introducing the endotype concept to address the challenge of disease heterogeneity in type 1 diabetes. *Diabetes Care* 43, 5–12 (2020).
- M. J. Redondo, N. G. Morgan, Heterogeneity and endotypes in type 1 diabetes mellitus. Nat. Rev. Endocrinol. 19, 542–554 (2023).
- C. McGrail, J. Chiou, R. Elgamal, A. M. Luckett, R. A. Oram, P. Benaglio, K. J. Gaulton, Genetic discovery and risk prediction for type 1 diabetes in individuals without high-Risk HLA-DR3/DR4 haplotypes. *Diabetes Care* 48, 202–211 (2025).
- A. Thibodeau, A. Eroglu, C. S. McGinnis, N. Lawlor, D. Nehar-Belaid, R. Kursawe,
 R. Marches, D. N. Conrad, G. A. Kuchel, Z. J. Gartner, J. Banchereau, M. L. Stitzel, A. E. Cicek,
 D. Ucar, AMULET: A novel read count-based method for effective multiplet detection from single nucleus ATAC-seq data. *Genome Biol.* 22, 252 (2021).
- G. X. Y. Zheng, J. M. Terry, P. Belgrader, P. Ryvkin, Z. W. Bent, R. Wilson, S. B. Ziraldo, T. D. Wheeler, G. P. McDermott, J. Zhu, M. T. Gregory, J. Shuga, L. Montesclaros, J. G. Underwood, D. A. Masquelier, S. Y. Nishimura, M. Schnall-Levin, P. W. Wyatt, C. M. Hindson, R. Bharadwaj, A. Wong, K. D. Ness, L. W. Beppu, H. J. Deeg, C. McFarland, K. R. Loeb, W. J. Valente, N. G. Ericson, E. A. Stevens, J. P. Radich, T. S. Mikkelsen, B. J. Hindson, J. H. Bielas, Massively parallel digital transcriptional profiling of single cells. Nat. Commun. 8, 14049 (2017).
- C. S. McGinnis, L. M. Murrow, Z. J. Gartner, DoubletFinder: Doublet detection in single-cell RNA sequencing data using artificial nearest neighbors. Cell Syst. 8, 329–337.e4 (2019).
- M. D. Young, S. Behjati, SoupX removes ambient RNA contamination from droplet-based single-cell RNA sequencing data. GigaScience 9, giaa151 (2020).
- R. Dries, Q. Zhu, R. Dong, C.-H. L. Eng, H. Li, K. Liu, Y. Fu, T. Zhao, A. Sarkar, F. Bao, R. E. George, N. Pierson, L. Cai, G.-C. Yuan, Giotto: A toolbox for integrative analysis and visualization of spatial expression data. *Genome Biol.* 22, 78 (2021).
- F. A. Wolf, P. Angerer, F. J. Theis, SCANPY: Large-scale single-cell gene expression data analysis. Genome Biol. 19, 15 (2018).
- Y. Hao, S. Hao, E. Andersen-Nissen, W. M. Mauck, S. Zheng, A. Butler, M. J. Lee, A. J. Wilk, C. Darby, M. Zager, P. Hoffman, M. Stoeckius, E. Papalexi, E. P. Mimitou, J. Jain, A. Srivastava, T. Stuart, L. M. Fleming, B. Yeung, A. J. Rogers, J. M. McElrath, C. A. Blish, R. Gottardo, P. Smibert, R. Satija, Integrated analysis of multimodal single-cell data. *Cell* 184, 3573–3587,e29 (2021).
- M. I. Love, W. Huber, S. Anders, Moderated estimation of fold change and dispersion for RNA-seq data with DESeq2. Genome Biol. 15, 550 (2014).
- M. Kanehisa, KEGG: Kyoto encyclopedia of genes and genomes. Nucleic Acids Res. 28, 27–30 (2000).
- M. Kanehisa, Toward understanding the origin and evolution of cellular organisms. Protein Sci. 28, 1947–1951 (2019).
- M. Kanehisa, M. Furumichi, Y. Sato, M. Kawashima, M. Ishiguro-Watanabe, KEGG for taxonomy-based analysis of pathways and genomes. *Nucleic Acids Res.* 51, D587–D592 (2023).
- M. Milacic, D. Beavers, P. Conley, C. Gong, M. Gillespie, J. Griss, R. Haw, B. Jassal, L. Matthews, B. May, R. Petryszak, E. Ragueneau, K. Rothfels, C. Sevilla, V. Shamovsky, R. Stephan, K. Tiwari, T. Varusai, J. Weiser, A. Wright, G. Wu, L. Stein, H. Hermjakob, P. D'Eustachio, The reactome pathway knowledgebase 2024. *Nucleic Acids Res.* 52, D672–D678 (2024).
- T. Stuart, A. Srivastava, S. Madad, C. A. Lareau, R. Satija, Single-cell chromatin state analysis with Signac. Nat. Methods 18, 1333–1341 (2021).
- Y. Zhang, T. Liu, C. A. Meyer, J. Eeckhoute, D. S. Johnson, B. E. Bernstein, C. Nusbaum, R. M. Myers, M. Brown, W. Li, X. S. Liu, Model-based Analysis of ChIP-Seq (MACS). Genome Biol. 9, R137 (2008).
- R. Lopez, J. Regier, M. B. Cole, M. I. Jordan, N. Yosef, Deep generative modeling for single-cell transcriptomics. *Nat. Methods* 15, 1053–1058 (2018).

- L. R. Nassar, G. P. Barber, A. Benet-Pagès, J. Casper, H. Clawson, M. Diekhans, C. Fischer, J. N. Gonzalez, A. S. Hinrichs, B. T. Lee, C. M. Lee, P. Muthuraman, B. Nguy, T. Pereira, P. Nejad, G. Perez, B. J. Raney, D. Schmelter, M. L. Speir, B. D. Wick, A. S. Zweig, D. Haussler, R. M. Kuhn, M. Haeussler, W. J. Kent, The UCSC Genome Browser database: 2023 update. Nucleic Acids Res. 51, D1188–D1195 (2023).
- S. Heinz, C. Benner, N. Spann, E. Bertolino, Y. C. Lin, P. Laslo, J. X. Cheng, C. Murre, H. Singh, C. K. Glass, Simple combinations of lineage-determining transcription factors prime cis-regulatory elements required for macrophage and B cell identities. *Mol. Cell* 38, 576–589 (2010).
- C. Y. McLean, D. Bristor, M. Hiller, S. L. Clarke, B. T. Schaar, C. B. Lowe, A. M. Wenger,
 G. Bejerano, GREAT improves functional interpretation of cis-regulatory regions. *Nat. Biotechnol.* 28, 495–501 (2010).
- D. Bates, M. Mächler, B. Bolker, S. Walker, Fitting linear mixed-effects models using Ime4. J. Stat. Softw. 67, 1–48 (2015).
- V. K. Mootha, C. M. Lindgren, K.-F. Eriksson, A. Subramanian, S. Sihag, J. Lehar,
 P. Puigserver, E. Carlsson, M. Ridderstråle, E. Laurila, N. Houstis, M. J. Daly, N. Patterson,
 J. P. Mesirov, T. R. Golub, P. Tamayo, B. Spiegelman, E. S. Lander, J. N. Hirschhorn,
 D. Altshuler, L. C. Groop, PGC-1α-responsive genes involved in oxidative phosphorylation are coordinately downregulated in human diabetes. *Nat. Genet.* 34, 267–273 (2003).
- A. Subramanian, P. Tamayo, V. K. Mootha, S. Mukherjee, B. L. Ebert, M. A. Gillette,
 A. Paulovich, S. L. Pomeroy, T. R. Golub, E. S. Lander, J. P. Mesirov, Gene set enrichment
 analysis: A knowledge-based approach for interpreting genome-wide expression
 profiles. *Proc. Natl. Acad. Sci. U.S.A.* 102, 15545–15550 (2005).
- B. Jassal, L. Matthews, G. Viteri, C. Gong, P. Lorente, A. Fabregat, K. Sidiropoulos, J. Cook, M. Gillespie, R. Haw, F. Loney, B. May, M. Milacic, K. Rothfels, C. Sevilla, V. Shamovsky, S. Shorser, T. Varusai, J. Weiser, G. Wu, L. Stein, H. Hermjakob, P. D'Eustachio, The reactome pathway knowledgebase. *Nucleic Acids Res.* 48, D498–D503 (2019).
- J. Griss, G. Viteri, K. Sidiropoulos, V. Nguyen, A. Fabregat, H. Hermjakob, ReactomeGSA

 efficient multi-omics comparative pathway analysis. Mol. Cell. Proteomics 19, 2115–2125

 (2020).
- A. Fabregat, K. Sidiropoulos, G. Viteri, P. Marin-Garcia, P. Ping, L. Stein, P. D'Eustachio, H. Hermjakob, Reactome diagram viewer: Data structures and strategies to boost performance. *Bioinformatics* 34, 1208–1214 (2018).
- A. Fabregat, F. Korninger, G. Viteri, K. Sidiropoulos, P. Marin-Garcia, P. Ping, G. Wu, L. Stein, P. D'Eustachio, H. Hermjakob, Reactome graph database: Efficient access to complex pathway data. *PLOS Comput. Biol.* 14, e1005968 (2018).
- K. Sidiropoulos, G. Viteri, C. Sevilla, S. Jupe, M. Webber, M. Orlic-Milacic, B. Jassal, B. May, V. Shamovsky, C. Duenas, K. Rothfels, L. Matthews, H. Song, L. Stein, R. Haw, P. D'Eustachio, P. Ping, H. Hermjakob, A. Fabregat, Reactome enhanced pathway visualization. *Bioinformatics* 33, 3461–3467 (2017).
- G. Wu, R. Haw, "Functional interaction network construction and analysis for disease discovery" in *Protein Bioinformatics*, C. H. Wu, C. N. Arighi, K. E. Ross, Eds. (Springer New York, 2017), vol. 1558 of *Methods in Molecular Biology*, pp. 235–253. http://link.springer. com/10.1007/978-1-4939-6783-4_11.
- M. Gillespie, B. Jassal, R. Stephan, M. Milacic, K. Rothfels, A. Senff-Ribeiro, J. Griss, C. Sevilla, L. Matthews, C. Gong, C. Deng, T. Varusai, E. Ragueneau, Y. Haider, B. May, V. Shamovsky, J. Weiser, T. Brunson, N. Sanati, L. Beckman, X. Shao, A. Fabregat, K. Sidiropoulos, J. Murillo, G. Viteri, J. Cook, S. Shorser, G. Bader, E. Demir, C. Sander, R. Haw, G. Wu, L. Stein, H. Hermjakob, P. D'Eustachio, The reactome pathway knowledgebase 2022. Nucleic Acids Res. 50, D687–D692 (2022).
- J. A. Castro-Mondragon, R. Riudavets-Puig, I. Rauluseviciute, R. Berhanu Lemma, L. Turchi, R. Blanc-Mathieu, J. Lucas, P. Boddie, A. Khan, N. Manosalva Pérez, O. Fornes, T. Y. Leung, A. Aguirre, F. Hammal, D. Schmelter, D. Baranasic, B. Ballester, A. Sandelin, B. Lenhard, K. Vandepoele, W. W. Wasserman, F. Parcy, A. Mathelier, JASPAR 2022: The 9th release of the open-access database of transcription factor binding profiles. *Nucleic Acids Res.* 50, D165–D173 (2022).
- C. P. Fulco, J. Nasser, T. R. Jones, G. Munson, D. T. Bergman, V. Subramanian,
 S. R. Grossman, R. Anyoha, B. R. Doughty, T. A. Patwardhan, T. H. Nguyen, M. Kane,
 E. M. Perez, N. C. Durand, C. A. Lareau, E. K. Stamenova, E. L. Aiden, E. S. Lander,
 J. M. Engreitz, Activity-by-contact model of enhancer–promoter regulation from thousands of CRISPR perturbations. *Nat. Genet.* 51, 1664–1669 (2019).
- H. Zhao, Z. Sun, J. Wang, H. Huang, J.-P. Kocher, L. Wang, CrossMap: A versatile tool for coordinate conversion between genome assemblies. *Bioinformatics* 30, 1006–1007 (2014).
- H. E. Arda, J. Tsai, Y. R. Rosli, P. Giresi, R. Bottino, W. J. Greenleaf, H. Y. Chang, S. K. Kim, A chromatin basis for cell lineage and disease risk in the human pancreas. *Cell Syst.* 7, 310–322.e4 (2018).
- A. T. Satpathy, J. M. Granja, K. E. Yost, Y. Qi, F. Meschi, G. P. McDermott, B. N. Olsen, M. R. Mumbach, S. E. Pierce, M. R. Corces, P. Shah, J. C. Bell, D. Jhutty, C. M. Nemec, J. Wang, L. Wang, Y. Yin, P. G. Giresi, A. L. S. Chang, G. X. Y. Zheng, W. J. Greenleaf, H. Y. Chang, Massively parallel single-cell chromatin landscapes of human immune cell development and intratumoral T cell exhaustion. *Nat. Biotechnol.* 37, 925–936 (2019).

- J. Nasser, D. T. Bergman, C. P. Fulco, P. Guckelberger, B. R. Doughty, T. A. Patwardhan, T. R. Jones, T. H. Nguyen, J. C. Ulirsch, F. Lekschas, K. Mualim, H. M. Natri, E. M. Weeks, G. Munson, M. Kane, H. Y. Kang, A. Cui, J. P. Ray, T. M. Eisenhaure, R. L. Collins, K. Dey, H. Pfister, A. L. Price, C. B. Epstein, A. Kundaje, R. J. Xavier, M. J. Daly, H. Huang, H. K. Finucane, N. Hacohen, E. S. Lander, J. M. Engreitz, Genome-wide enhancer maps link risk variants to disease genes. Nature 593, 238–243 (2021).
- J. Wakefield, Bayes factors for genome-wide association studies: Comparison with P-values. Genet. Epidemiol. 33, 79–86 (2009).
- UniProt Consortium, UniProt: The universal protein knowledgebase in 2023. Nucleic Acids Res. 51, D523–D531 (2023).
- G. Stelzer, N. Rosen, I. Plaschkes, S. Zimmerman, M. Twik, S. Fishilevich, T. I. Stein, R. Nudel, I. Lieder, Y. Mazor, S. Kaplan, D. Dahary, D. Warshawsky, Y. Guan-Golan, A. Kohn, N. Rappaport, M. Safran, D. Lancet, The GeneCards suite: From gene data mining to disease genome sequence analyses. *Curr. Protoc. Bioinformatics* 54, 1.30.1–1.30.33 (2016).
- 102. M. Safran, N. Rosen, M. Twik, R. BarShir, T. I. Stein, D. Dahary, S. Fishilevich, D. Lancet, "The GeneCards suite" in *Practical Guide to Life Science Databases*, I. Abugessaisa, T. Kasukawa, Eds. (Springer Nature Singapore, 2021), pp. 27–56. https://link.springer. com/10.1007/978-981-16-5812-9_2.
- R. Patro, G. Duggal, M. I. Love, R. A. Irizarry, C. Kingsford, Salmon provides fast and bias-aware quantification of transcript expression. *Nat. Methods* 14, 417–419 (2017).
- C. Soneson, M. I. Love, M. D. Robinson, Differential analyses for RNA-seq: Transcript-level estimates improve gene-level inferences. F1000Res 4, 1521 (2015).

Acknowledgments: The content and views expressed are the responsibility of the authors and do not necessarily reflect the official view of nPOD. Organ Procurement Organizations (OPO) partnering with nPOD to provide research resources are listed at https://npod.org/ for-partners/npod-partners/. This manuscript used data acquired from the HPAP (HPAP-RRID:SCR_016202) Database (https://hpap.pmacs.upenn.edu), a Human Islet Research Network (RRID:SCR_014393) consortium (UC4-DK-112217, U01-DK-123594, UC4-DK-112232, and U01-DK-123716). Funding: The work in this study was funded by DK120429 and DK122607 to K.J.G. and M.S. and T32 GM00866 to R.M. This research was performed with the support of the nPOD (RRID:SCR_014641), a collaborative T1D research project supported by JDRF (nPOD: 5-SRA-2018-557-O-R) and The Leona M. & Harry B. Helmsley Charitable Trust (grant no. 2018PG-T1D053), Author contributions: K.J.G.: Conceptualization, methodology, visualization, data curation, formal analysis, funding acquisition, project administration, supervision, writing—original draft, and writing—review and editing. R.M.: Conceptualization, methodology, investigation, visualization, data curation, formal analysis, software, writingoriginal draft, and writing—review and editing, S.J.: Methodology, investigation, visualization, data curation, formal analysis, software, resources, validation, writing—original draft, and writing—review and editing. W.E.: Formal analysis, software, and visualization. L.T.: Investigation, formal analysis, visualization, validation, writing—original draft, and writing—review and editing. A.H.: Formal analysis, visualization, software, and writing—review and editing. H.M.: Methodology and software. R.E.: Methodology, data curation, resources, and software. M.M.: Methodology and investigation. D.B.: Investigation. E.G.: Investigation and formal analysis, K.K.: Data curation and software, C.M.: Formal analysis, conceptualization, and writing—review and editing. K.V.: Investigation, validation, resources, and writing—review and editing. J.C.: Formal analysis. E.B.: Formal analysis and software. I.K.: Resources. M.A.: Investigation, funding acquisition, resources, and writing—review and editing. G.W.: Methodology. C.Z.: Resources. S.P.: Methodology, project administration, supervision, and writing—review and editing. F.J.T.: Conceptualization, methodology, funding acquisition, project administration, software, supervision, and writing—review and editing. M.S.: Conceptualization, methodology, validation, funding acquisition, resources, project administration, supervision, and writing—review and editing. Competing interests: The following conflicts of interest are reported for several authors, K.J.G. has done consulting for Genentech, received honoraria from Pfizer, and holds stock in Neurocrine Biosciences, and his spouse is employed by Altos Labs Inc. J.C. and R.E. hold stock in and are employed by Pfizer Inc. F.J.T. consults for Immunai, Singularity Bio, CytoReason, Cellarity, and Omniscope and has ownership interest in Dermagnostix and Cellarity. All other authors declare that they have no competing interests. Data and materials availability: Raw sequence data can be accessed from GEO at accession numbers GSE273594, GSE273597, and GSE273598, and spatial imaging data can be accessed from Zenodo at doi:10.5281/zenodo.14870960. Supplementary data and visualization of single-cell and spatial maps can be accessed at https://www.gaultonlab.org/ pages/T1D-pancreas-genomics/. Supplementary data files can be accessed from Zenodo at doi:10.5281/zenodo.15802028. Code is archived in Zenodo at 10.5281/zenodo.15832080 and available as an additional resource at https://github.com/Gaulton-Lab/nPOD and https:// github.com/theislab/spatial pancreas.

Submitted 20 April 2025 Accepted 8 August 2025 Published 10 September 2025 10.1126/sciadv.ady0080